# "Analytical Modeling for Sliding Friction of Rubber-Road Contact"

Sunish Vadakkeveetil

Thesis submitted to the faculty of the Virginia Polytechnic Institute and State University in partial fulfillment of the requirements for the degree of

Master of Science

In

Mechanical Engineering

Saied Taheri

Corina Sandu

John B Ferris

April 21, 2017

Blacksburg, VA

Keywords: Rubber Friction, Hysteresis Friction, Adhesion Friction, Profile Measurement, Analytical model, Tire friction

# Analytical Modeling for Sliding Friction of Rubber-Road Contact

*Sunish Vadakkeveetil*

## ABSTRACT

Rubber friction is an important aspect to tire engineers, material developers and pavement engineers because of its importance in the estimation of forces generated at the contact, which further helps in optimizing tire and vehicle performances, and to estimate tire wear. It mainly depends on the material properties, contact mechanics and operating condition. There are two major contributions to rubber friction, due to repeated viscoelastic deformation from undulations of surface called hysteresis and due to Vander Waals interaction of the molecules called adhesion. The study focuses on analytical modeling of friction for stationary sliding of rubber block on rough surfaces. Two novel approaches are discussed and compared. Frictional shear stress is obtained from the energy dissipated at the contact interface due to the elastic deformations of rubber block at different length scales. Contact mechanics theories based on continuity approach combined with stochastic processes to estimate the real contact area, mean penetration depth and true stresses at contact depending on operating conditions. Rubber properties are highly temperature dependent. Temperature model developed based on heat diffusion relation is integrated to consider the effects of temperature rise due to frictional heating.

Model results are validated with theoretical results of literature. Simulation results of friction model is obtained for Compound A sliding on rough surface. Material properties are obtained using Dynamic Mechanical Analysis and Time temperature superposition. Influence of the friction models under different conditions are discussed. Model results are validated with experimental data from Dynamic friction tester on a 120-grit surface followed by future works.

# Analytical Modeling for Sliding Friction of Rubber-Road Contact

*Sunish Vadakkeveetil*

## GENERAL AUDIENCE ABSTRACT

Friction is a complex phenomenon that occurs in all tribological application. It is termed as the ratio of the shear force resisting the motion of the component to the normal force acting on the component. Microscopic observation has observed the importance of the effective contact area and roughness of the substrates in the influence of the friction.

Rubber friction is an important aspect to tire engineers, material developers and pavement engineers because of its importance in the estimation of forces generated at the contact, which further helps in optimizing tire and vehicle performances, and to estimate tire wear. Because of the viscoelastic nature of rubber, the friction in rubber is much more complicated than observed for elastic materials and hence depends on the material properties apart from contact mechanics and operating condition. There are two major contributions to rubber friction, due to repeated viscoelastic deformation from undulations of surface called hysteresis and due to Vander Waals interaction of the molecules called adhesion. The study focuses on analytical modeling of friction for stationary sliding of rubber block on rough surfaces. Two novel approaches are discussed and compared. Frictional shear stress is obtained from the energy dissipated at the contact interface due to the elastic deformations of rubber block at different length scales. Contact mechanics theories based on continuity approach combined with stochastic processes to estimate the real contact area, mean penetration depth and true stresses at contact depending on operating conditions. Rubber properties are highly temperature dependent.

Temperature model developed based on heat diffusion relation is integrated to consider the effects of temperature rise due to frictional heating.

Model results are validated with theoretical results of literature. Simulation results of friction model is obtained for Compound A sliding on rough surface. Material properties are obtained using Dynamic Mechanical Analysis and Time temperature superposition. Influence of the friction models under different conditions are discussed. Model results are validated with experimental data from Dynamic friction tester on a 120-grit surface followed by future works.

# DEDICATION

*To my Parents, God the Almighty and my sister…*

## ACKNOWLEDGEMENT

I would like to first thank my parents for their support and encouragement. I would like to express my extreme gratitude towards my mentor and advisor Dr. Saied Taheri who not only provided me with the opportunity to explore the world of Tires but also for sharing his knowledge and experience, and for his insightful guidance throughout my graduate studies.

I would also like to thank my committee members: Dr. John Ferris and Dr. Corina Sandu for their encouragement and comments on the project. Special thanks to Mehran for sharing his knowledge and experience on Surface profile characterization and friction modeling.

I thank my project mates Anahita and Chuang for their useful discussion and support during the experimental measurements. I would like to thank Bridgestone for providing experimental data for the material properties of Compound A. I would like to thank all the industry mentors for the technical discussions and suggestions. I would also like to thank Center for Tire Research (CenTiRe) Organization and National Science Foundation (NSF) for providing the financial support. Finally, I thank my family and all my friends for their enthusiasm and motivation.

# TABLE OF CONTENTS

# LIST OF SYMBOLS

$\mu$ – Friction Coefficient

$\zeta$ – Magnification

$\rho$ – Density

$F_f$ – Frictional shear stress

$F_N$ – Normal Load

$v$ – Sliding Velocity

$E'$ - Storage Modulus

$E$" – Loss Modulus

$\omega$ – Angular frequency

$\tan\delta$ – Loss factor

$\tau$ – Characteristic time

$\Delta E$ – Energy dissipation

$\sigma_0$ – Nominal Pressure

$\nu$ – Poisson's Ratio

$\delta$ – Penetration depth

$d$ – Surface distance

$\phi(z)$ – Height distribution

$P(q)$ – Area ratio

$D$ – Heat Diffusivity

$\lambda$ – Length scale

$q$ – Wave vector $(2\pi/\lambda)$

$C_v$ – Specific heat

$D_f$ – Fractal Dimension

$H$ – Hurst Exponent

$\mu_A$ – Adhesion Friction Coefficient

$\mu_H$ – Hysteresis Friction Coefficient

$C_z(\lambda)$ – Height Difference Correlation Function

$p(\sigma, \zeta)$ – Stress Probability Distribution

$c_T$ – Transverse wave speed

$c_L$ – Longitudnal wave speed

$\lambda_{min}$ – Minimum length scale

$\langle z_p \rangle$ – Mean penetration depth

$N_s$ – Summit height density

$a_T$ – Horizontal shift factor

$E_a$ – Activation Energy

$A_0$ – Nominal contact area

$\sigma_y$ – Yield stress; $\sigma_f$ – Frictional shear stress

$T_q$ – Temperature at different length scale

$q_0$ – Low cut off wave vector

$q_1$ – Large cut off wave vector

$\phi_s(z)$ - Summit height distribution

$C(q)$ – Surface roughness power spectrum

$F_n(t)$ – Greenwood Williamson Function

$R$ – Asperity radius of curvature

$\xi_{\parallel}, \lambda_0$ - Maximum length scale

$\xi_{\perp}, h_0$ - RMS roughness amplitude

$\dot{Q}$ – Heat generated at the contact interface

$\lambda_k$ – Thermal Conductivity

# LIST OF FIGURES

# LIST OF TABLES

# 1. INTRODUCTION

## 1.1.MOTIVATION

Contact friction is an inevitable phenomenon that occurs in all tribological application. The mechanisms of the rubber friction are different and more complex as compared to other materials due to frequency dependent viscoelastic nature of the material. Rubber friction is crucial in tire applications because of its importance in estimating the forces generated at the contact. Friction in tires is responsible for providing traction and comfort to the vehicle. However, in the contrary it also gives rise to rolling resistance and results in tire wear. Experimental observations [1-4] has shown the various factors that influence the rubber friction like normal load, sliding velocity, temperature, material properties, nature of surface and environmental condition. Developments in the contact mechanics theories has gathered interest among material developers, tire engineers and pavement engineers for a physics based friction model based on the friction mechanism, contact mechanics and surface roughness parameters. Henrich, Persson and Kluppel are pioneers in this area who developed friction models for hysteresis friction based on energy dissipation due to deformation at the rubber – road from surface roughness at different length scales. Past research in CenTiRe have focused on developing the surface characterization techniques that can be used to predict friction coefficient using the physics based model approach. It is very important to understand the physics behind the existing friction model and the various parameters used for the model in order for the development of a more proficient friction model by overcoming the assumptions of the existing models. A physics based model will be helpful for a more robust and efficient prediction of the friction coefficient under change in conditions unlike empirical relations that are highly dependent on the conditions at

which the fitting is performed – for a small change in a condition, the experiments and data fitting ought to be repeated.

## 1.2.RESEARCH CONTRIBUTION

Henrich, Persson and Kluppel are pioneers in the area of friction and contact mechanics. They have developed physics based friction models as a function of the material properties, sliding velocity, surface roughness and temperature. Our aim is to understand the physics behind the friction model, input parameters and the assumptions of the model. Different techniques used to obtain the input parameters of the model like the contact mechanics and material properties are discussed. Variation of the model under different conditions of surface roughness parameters, material properties are discussed in order to understand the behavior of the model to these parameters. Effect of frictional heating on the friction coefficient using a heat diffusion relation is integrated to consider the effect of temperature rise. The simulation results for Compound A on a 120-grit surface is compared with the experimental results.

## 1.3.DOCUMENT OUTLINE

**Chapter 2** explains a background on contact friction with emphasis on rubber friction. Viscoelastic nature of the material is explained. Experimental observation of rubber friction in the past is discussed to provide the influential factors and major contributions on rubber friction. Empirical models based on experimental observations are mentioned followed by a discussion on qualitative and quantitative modeling of friction.

**Chapter 3** focusses on the theoretical procedure to obtain the contact mechanics parameters, physics behind the development of the two friction models and the input

parameters required for the same. Theoretical comparison between the models is also discussed.

**Chapter 4** provides the experimental data obtained for successful simulation of the model that includes Dynamic mechanical analysis, estimation of surface profile using Nanovea profilometer and experimental friction coefficient with Dynamic friction tester.

**Chapter 5** shows characterization of the input parameters from the experimental data, simulation results for the general case and for the case of compound A sliding on 120-grit surface, influence of the model on various parameters and finally comparison of the results with the experimental data that is followed by some conclusion and future works. Appendix provides certain theoretical derivations of certain approaches.

Finally, providing the conclusions of the study with some future works for improvement of the model.

## 2. BACKGROUND

Frictional force is the resisting force, which acts on the contact interface when two bodies are moving in contact as shown in Figure 2.1. Research in understanding the mechanism of the friction has been going on for decades. Leonardo da Vinci stated – 'the frictional force is proportional to the normal load acting at the interface and it is independent of the apparent area of contact.' Amontons (1699) & Coulomb (1785) later formulated an empirical form to predict the friction coefficient as given by Eq. (2.1), where $F_f$ is the frictional force and $F_N$ the normal load and is still widely used.

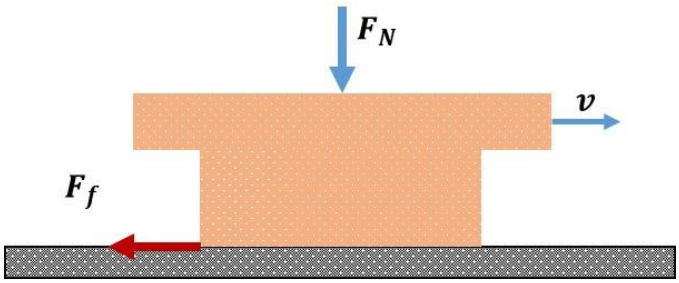


**FIGURE 2.1: FRICTIONAL FORCE BETWEEN TWO BODIES**

$$\mu = \frac{F_f}{F_N} \tag{2.1}$$

Bowden & Tabor[5] investigated the microscopic behavior of the contact where he found that the effective contact area is only a part of the nominal area and observed the deformation and relaxation of interlocking asperities that later was referred to as the stick slip oscillations due to the instabilities during steady sliding velocities. They classified the friction in the contact into static $(\mu_s)$ and dynamic friction coefficient$(\mu_d)$. Static friction often occurs at very low sliding velocities and up until the pull force causes no movement of the bodies in contact. It can also be referred to as the friction during the stick portion of the body. In addition, the more the body is in rest the higher is the static friction coefficient. Kinetic or dynamic friction depends on the steady sliding velocity. There is no universal behavior and we can observe a

decrease or increase in friction with change in velocity referred to as the velocity weakening and velocity strengthening effect. Friction dynamics in viscoelastic materials often exhibit hysteretic response and hence depends on the memory effects [6].

## 2.1. VISCOELASTIC MATERIAL PROPERTIES

Viscoelastic materials have a combination of elastic and viscous parts and the response of the material is always time dependent. These materials are represented using a combination of linear elastic springs, for its elastic response and linear dashpots, for the viscous part. It has a complex modulus that is dependent on time rate or frequency as shown in Figure 2.4 and given by Eq. (2.2), the real part of the modulus is called the storage modulus and the imaginary part is the loss modulus mainly due to molecular rearrangements. An application of sinusoidal stress on a viscoelastic material will result in a sinusoidal strain but will be out of phase with the strain lagging the stress. This phase difference between stress and strain is referred to as the loss factor ($\tan\delta$) and is often given by the ratio of the loss and storage modulus as shown in Eq. (2.3).

$$E^* = E' + iE" \tag{2.2}$$

$$\tan\delta = \frac{E"(\omega)}{E'(\omega)} \tag{2.3}$$

Where $E'$ is the storage modulus, $E"$ is the loss modulus

The complex dynamic moduli of the viscoelastic material is obtained either by using linear constitutive models [7] or by experimental methods like dynamic mechanical analysis [8]. Some of the linear constitutive models, which are used for rubber, are the Kelvin Voigt model, Zener slider or Standard linear model (Voigt form). The

mechanics of materials and constitutive relations are used to obtain the modulus from the linear models.

**Kelvin-Voigt Model:** This is the simplest case of viscoelastic solid that is represented using a linear pair of spring and dashpot as shown in Figure 2.2. Using stress balance and constitutive relation the effective complex modulus of the material is given by,

$$E(\omega) = E + i\omega\eta \tag{2.4}$$

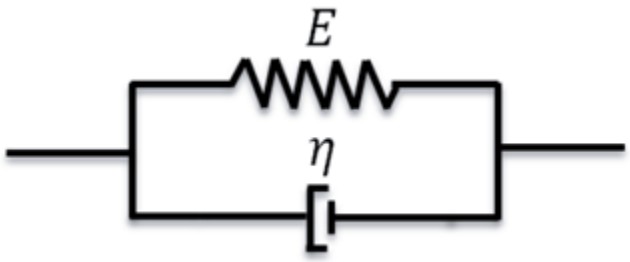


**FIGURE 2.2: KELVIN-VOIGT MODEL**

**Zener slider**: This is also called the standard linear viscoelastic solid. It is represented with a single spring and a Maxwell element in parallel to represent the viscoelastic behavior of rubber as shown in Figure 2.3(A). The mathematical relation for complex moduli is given by Eq. (2.5),

$$E(\omega) = \frac{(E_2E_1^2 + (E_1 + E_2)\omega^2\eta^2)}{E_1^2 + \omega^2\eta^2} + i\frac{\omega\eta}{E_1^2 + \eta^2\omega^2}E_1^2 \tag{2.5}$$

**Standard linear model (Voigt form):** In this case, the spring is in series with a Kelvin Voigt model as shown in Figure 2.3(B). This closely resembles the behavior of the viscoelastic solid that has an instantaneous response or rapid response. For example, rubber. The mathematical relation for complex moduli is given by Eq. (2.6),

$$E(\omega) = \frac{E_1(1 - i\omega\tau)}{1 + a - i\omega\tau}; \quad \tau = \frac{1}{\eta}; \quad a = \frac{E_1}{E_2} \tag{2.6}$$

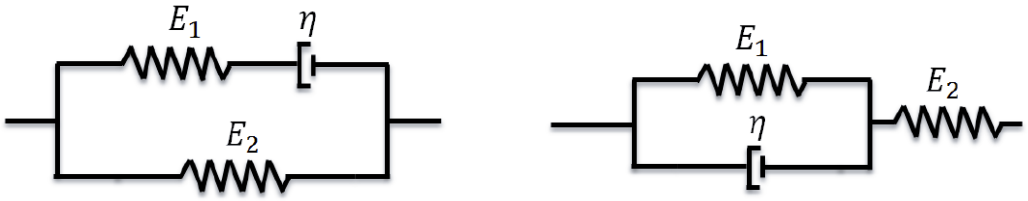


**FIGURE 2.3: (A) ZENER SLIDER (LEFT), (B) STANDARD LINEAR MODEL (VOIGT FORM) (RIGHT)**

Experimental testing using Dynamic Mechanical Analysis[9] can also be done in order to obtain the complex modulus of the viscoelastic materials. In the case of rubber, it is very important to obtain the modulus in a very wide range of frequencies to notice all three regions (rubbery, transition and glassy) as shown in Figure 2.4. However, it is not feasible to do testing at very low and very high frequencies because of instrument capabilities. Hence in order to obtain the elastic modulus at these wide frequency ranges Time-Temperature Superposition[10, 11] is applied.

The complex moduli are dependent on the temperature and composition of the material. Experiments has shown that the complex material moduli curve shifts to higher or lower frequencies with change in temperature in horizontal and vertical direction. Based on the experimental observations William Landel Ferry [12] developed empirical formulation for horizontal shift factor depending on the reference or glass transition temperature. It seemed to hold well for temperatures in the range of $100^oC$ above the glass transition temperature. Later, Arrhenius[10] developed a relationship to obtain the shift factor for temperature below the glass transition temperature.

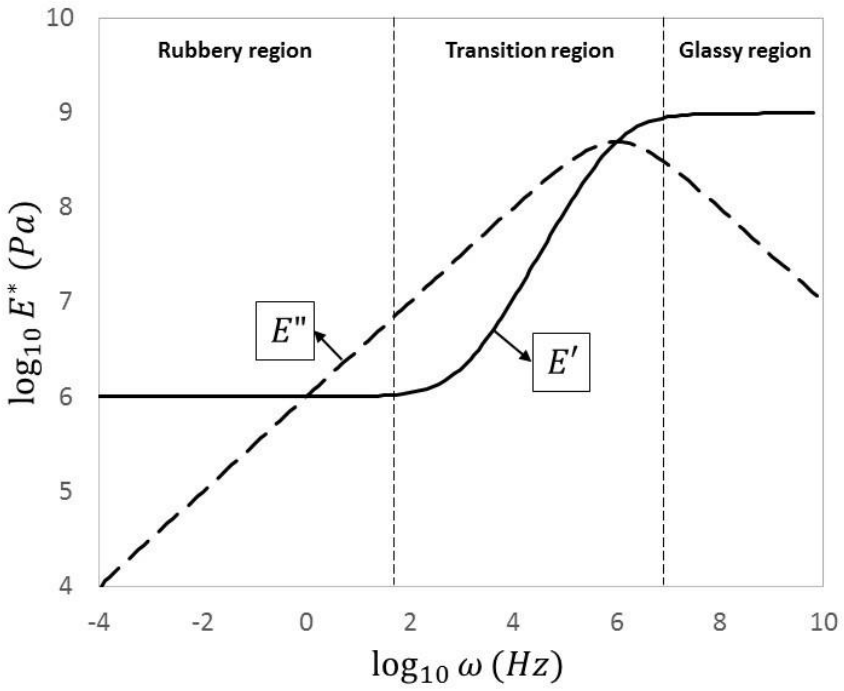


**FIGURE 2.4: VISCOELASTIC DYNAMIC MODULUS**

## 2.2.RUBBER FRICTION

Rubber friction fails to obey the classical laws of friction due to its inherent behavior compared to other solids such as dynamic moduli, internal damping and temperature dependence. Study of rubber friction is of considerable importance because of its wide usage in contact applications, e.g. construction of tires, bushings, wiper blades, footwear etc. Initial studies focused on the experimental observation of rubber friction under different conditions. Roth, Driscoll and Holt (1942) and Thirion (1946) [1] performed experiments on rubber compounds to understand the influence of sliding velocity and normal load respectively. Schallamach [1, 2] extended the experiments of rubber compound on ground glass and observed the variation of the friction coefficient and real area of contact with normal load as shown in Figure 2.5. Comparison of the theoretical results obtained using the Hertz theory seems to agree well at higher load, but deviated at lower loads due to the assumption of identical asperities at which the rubber is in contact at the tall asperities.

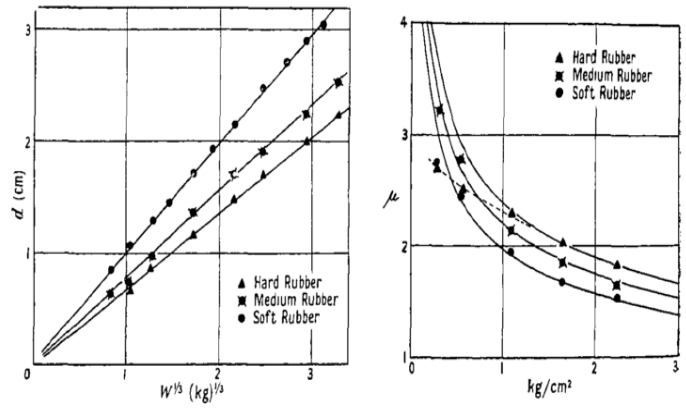


**FIGURE 2.5: LOAD DEPENDENCE OF REAL AREA OF CONTACT(RIGHT) AND FRICTION OF RUBBER (LEFT) [1]**

Based on the experimental evidences, Grosch [4] suggested the influence of viscoelastic behavior on the rubber friction. He conducted experiments using different rubber compounds on different surfaces and related the temperature and velocity dependence of the rubber friction to rate and temperature dependence of the viscoelastic material using the WLF transform [12].

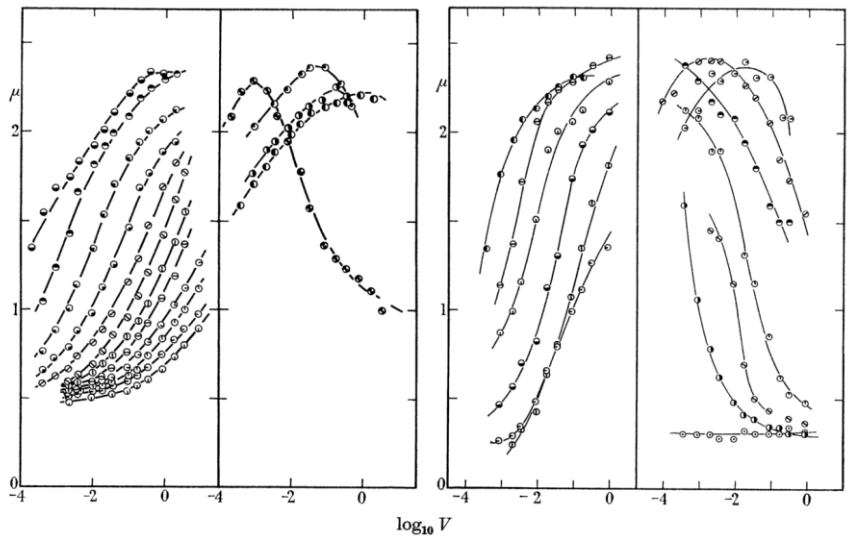


**FIGURE 2.6: VELOCITY AND TEMPERATURE DEPENDENCY OF RUBBER FRICTION [4]**

Friction variation for different surfaces observed the different contribution of friction. Two peaks was observed in the case of rough surface, one due to the deformation losses (at higher velocity) and the other due to the molecular adhesion (at lower velocity) of the rubber to the surface which increases the longer the material stays at rest [1, 4, 13] as shown in Figure 2.7. Depending on the surface and the conditions of the surface, the number of peaks are effected. The type and composition of the material also seem to effect a specific friction peak. Crystallized material seems to effect the adhesion component more due to the variation in the molecular structure whereas the filler concentration decreased the friction due to deformation losses rapidly because of its effect on the loss modulus.

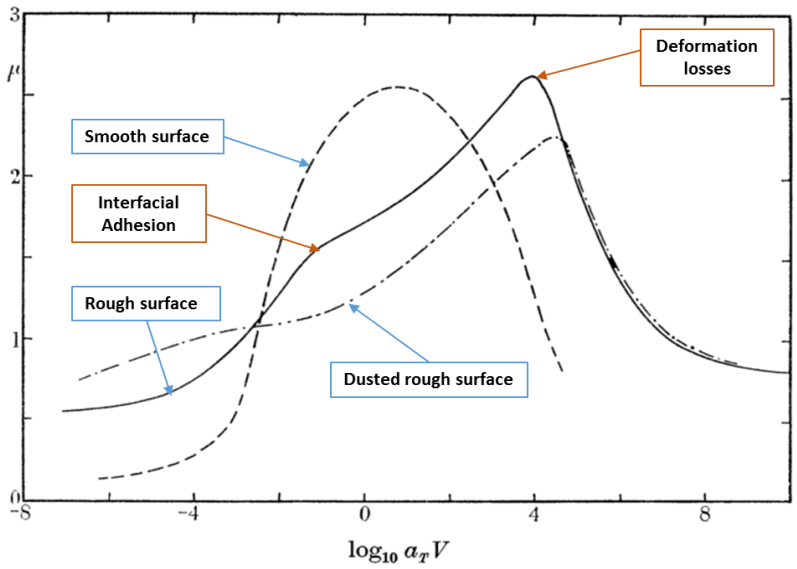


**FIGURE 2.7: MAJOR CONTRIBUTIONS TO RUBBER FRICTION AND INFLUENCE OF ROAD SURFACE [4]**

## Factors Effecting Rubber Friction

Depending on the experimental observations, we can obtain the various factors that influence the friction coefficient and its contributions.

- Normal load and real area of contact

- Sliding velocity and Temperature
- Viscoelastic material properties – Frequency and temperature dependent complex moduli
- Nature of surface – Degree of roughness of the surface
- Presence of contamination layer or lubrication on the surface

**Types of rubber friction**

Based on the experimental studies, the major contribution to the friction coefficient is from the deformation losses and the molecular adhesion,

$$\mu = \mu_A + \mu_H \tag{2.7}$$

$\mu_A$ is the adhesion component of friction that is mainly due to the molecular interaction of the rubber with the surface during sliding. It is due to the deformation of the molecular chain in contact with the surface that stretches until it reaches its maximum potential, breaks from the surface and re-attaches at a different location after relaxation, as shown in Figure 2.8(A). Mainly dependent on the contact interface properties it is dominant on smooth surface under low velocities and high loads. Surface contamination or lubrication can reduce this contribution.

$\mu_H$ is the hysteresis component of friction that is mainly due to the deformation losses in the rubber during sliding as shown in Figure 2.8(B). It is due to the internal friction of rubber because of the oscillating forces exerted from the undulation of the surface during sliding. A material dependent component solely due to the loss modulus or the imaginary part of the complex dynamic moduli. It is mainly dependent on the surface roughness and is dominant under high sliding velocities on rough surface. The contribution of this component is reduced by changing the loss modulus or sliding on a dry and smooth surface.

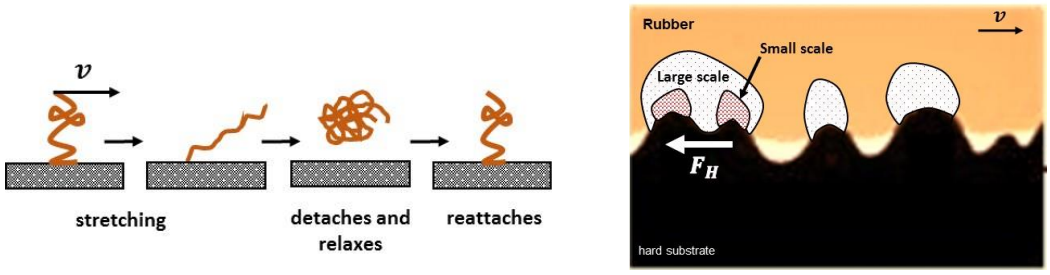


**FIGURE 2.8: (A) ADHESION FRICTION PROCESS, (B) – HYSTERESIS FRICTION AND ENERGY DISSIPATION AT DIFFERENT LENGTH SCALES**

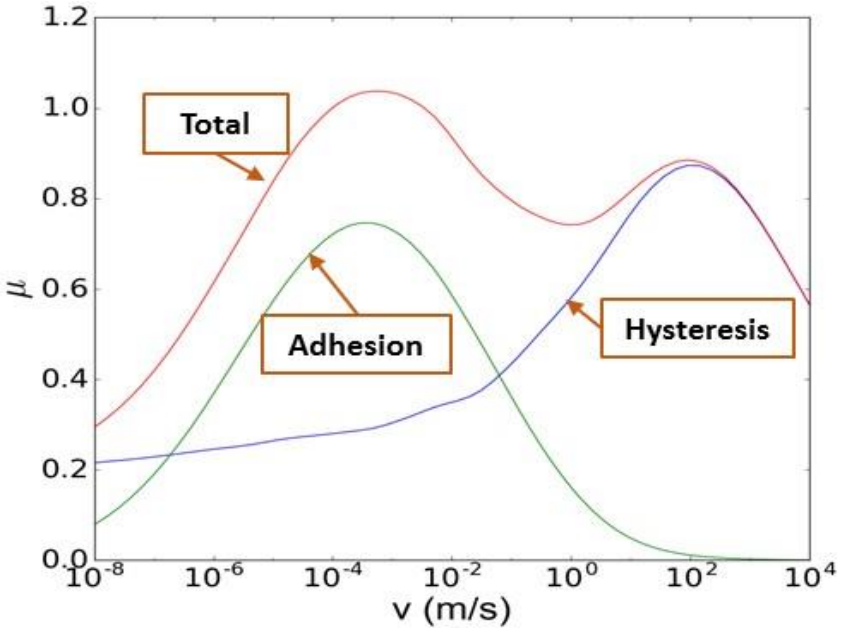


**FIGURE 2.9: MAJOR CONTRIBUTION OF FRICTION USING RESULTS**

The other physical mechanism, the cohesion component $\mu_c$ responsible for the wear process at interface and occurs for surfaces with sharp asperities. The viscous component $\mu_v$ due to the lubrication at the contact interface which depends on the viscosity of the fluid and nature of contact.

## 2.3.EMPIRICAL FRICTION MODEL

Based on the experimental studies [1, 2, 4, 14], empirical models were developed in order to predict the friction coefficient at the contact interface as a function of the different parameters. These models are extensively used for ranking of compounds

[15], Finite element analysis of tire [16-19] and vehicle dynamic simulations because of its accuracy and efficiency for a specific condition. The various empirical models are as shown in Table 2.1. Though efficient in obtaining the result, it is restricted to the condition at which the experimental data was obtained and fitting performed which has to be repeated if a condition changes.

**TABLE 2.1: SEMI EMPIRICAL FRICTION EQUATION**

| Empirical Model | Equation | Significance |
|---|---|---|
| **Schallamach [1]** | $\mu = \mu_0 \left\{\frac{p}{p_0}\right\}^{-1/3}$ | Obtains the friction coefficient as a function of normal load |
| **Savkoor [14]** | $\mu(v) = \mu_s + (\mu_m - \mu_s)\exp\left\{-h^2 \log^2\left(\frac{v}{V_{max}}\right)\right\}$ | Obtains the friction coefficient as a function of sliding speed and also includes the adhesion and hysteretic component |
| **Lugre [20]** | $F_f(V,Z) = \sigma_0 Z + \sigma_2 V + \sigma_1\left(V - \frac{\sigma_0\lvert V\rvert}{\left[F_c + (F_s - F_c)e^{-\left(\frac{V}{V_s}\right)^2}\right]}\right)$ | Considers the frictional interface as spring/damper model and obtains the frictional force as a function of deflection and sliding speed. |

| | | |
|---|---|---|
| **Huemer [18]** | $\mu = \dfrac{\alpha\lvert p\rvert^{n-1} + \beta}{a + \dfrac{b}{\lvert v\rvert^{\frac{1}{m}}} + \dfrac{c}{\lvert v\rvert^{\frac{2}{m}}}}$ | Considers the dependence of frictional surface, rubber compound and shape of block. |
| **Rado [20]** | $\mu = \mu_p . e^{-\left(\frac{\ln\left(\frac{V}{V_{peak}}\right)}{C}\right)^2}$ | Obtains the friction coefficient as a function of slip speed for transient condition. |
| **B. Lorenz [21]** | $\mu_{adh} = \dfrac{\tau_{f0}}{\sigma_0} \exp\left(-c\left[\log_{10}\left(\dfrac{v}{v_0}\right)\right]^2\right) P(q)$ | Semi empirical model to estimate the adhesion friction as a function of sliding velocity and length scale. |

## 2.4.ANALYTICAL FRICTION MODEL

Depending on the experimental observations, influential factors and the mechanism of friction models based on the physics at the contact interface were observed. In order to obtain an accurate friction model, it is important to define the contact parameters. Hertz (1886) [22] first developed a contact theory for two curved smooth surfaces as shown in Figure 2.10(A) in contact based on continuity approach and obtained the true area of contact, penetration depth and normal stress. However, in general the surfaces are considered rough at micro scale. Hence, Greenwood Williamson [23] developed a theory for a nominally flat surface considering the asperities spherical with identical radius but at different heights following a Gaussian height distribution as shown in Figure 2.10 (C). Johnson-Kendall-Robert

(JKR) [24] considered adhesion at the contact and obtained the pull off force based on the interfacial energy of the contact interface as shown in Figure 2.10 (B). Bush et al [25] extended the GW theory by considering the statistical variation of radius of asperities as shown in Figure 2.10(D) and using the random process theory to obtain the distribution of height and radius of curvature. He used spectral analysis to define the contact and considered different length scales.

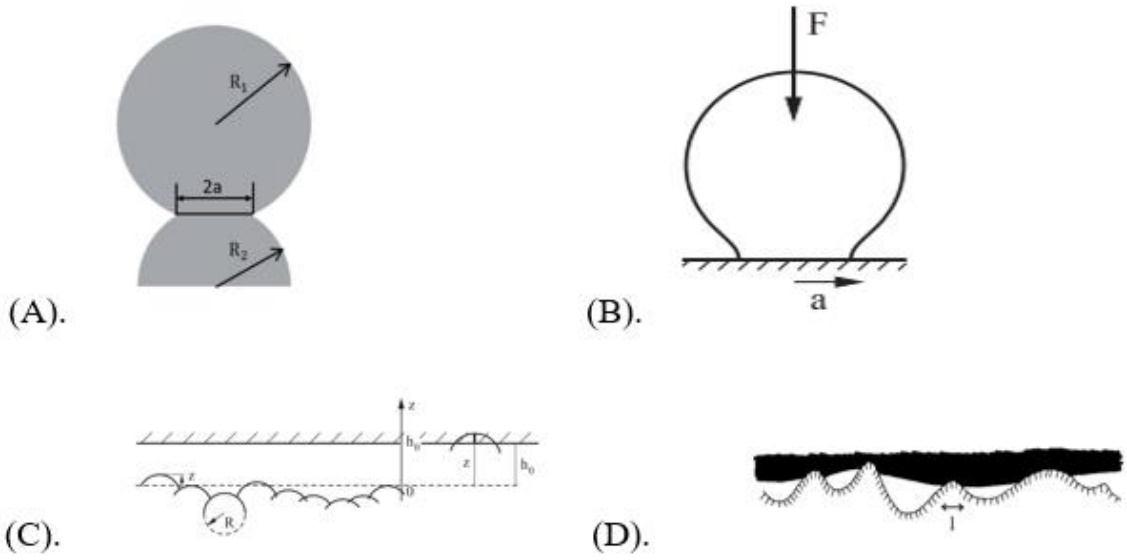


**FIGURE 2.10: (A) HERTZ CONTACT THEORY, (B) JKR THEORY, (C) GREENWOOD-WILLIAMSON THEORY, (D) VARYING ASPERITIES**

Friction due to the deformation losses are obtained based on the energy dissipated from the elastic deformation of the material and relating the energy to the frictional shear stresses generated at the surface given by the Eq. (2.8, 2.9) [13, 26].

$$\Delta E = \int d^3x\, dt\, \dot{\boldsymbol{u}} \,.\, \sigma \tag{2.8}$$

$$\mu_H = \frac{\Delta E}{L\, v\, t} \tag{2.9}$$

Henrich [26] developed the hysteresis friction model considering the fractal nature of the surface, considering the GW theory to obtain the contact mechanics, and

considering the total energy as sum over different length scales. Kluppel [27] later extended the theory to consider and extension of GW theory to consider the perturbation of neighboring asperities. Persson [28] considers that the friction due to the deformation losses to be independent of the normal load. The general form of the hysteresis friction as obtained by Persson [13] is given by Eq. (2.10), where C is the surface roughness dependent parameter and hence the friction coefficient is considered to depend on the loss modulus of the material and the surface roughness parameter.

$$\mu_H = -C\ Im \frac{E(\omega)}{|E(\omega)|} \tag{2.10}$$

Though Persson and Kluppel uses the same phenomenon to obtain the hysteresis friction, they differ in their contact mechanics theory and the constitutive relation that will be discussed in the next section.

# 3. THEORETICAL APPROACH TOWARDS MODELING FRICTION

In this section, we discuss the physics behind the development of the friction model and contact mechanics. A brief description of the contact mechanics theories is given, followed by the characterization of the surface roughness profile. The theoretical approach of Persson and Kluppel's friction model is considered with comparison of the models.

## 3.1. CONTACT MECHANICS THEORIES

Contact mechanics is the study of deformation of bodies occurring at the contact interface due to relative motion of the bodies with respect to each other. All surfaces appeared to be smooth to the naked eyes, possess some level of roughness at higher magnifications as shown in Figure 3.1. The roughness of the surface causes variation in the real area of contact, pressure distribution and deformation of the bodies in contact due to change in the normal load, sliding velocity, material properties of both bodies. It is very complex to predict the contact mechanics parameters and its variation to the input parameters by including the surface profile of both bodies. Various contact mechanics theories were developed based on continuum mechanics or theory of elasticity approaches assuming linear elastic isotropic medium.

### Hertz Contact Theory

It predicts the contact mechanics of two perfectly smooth non-confirming elastic half spaces. The deformations are obtained by assuming point contact on an elastic

half space with no tangential motion as shown in Figure 3.2. A boundary condition for no penetration of the surface for point in contact is considered by the Eq. (3.1)

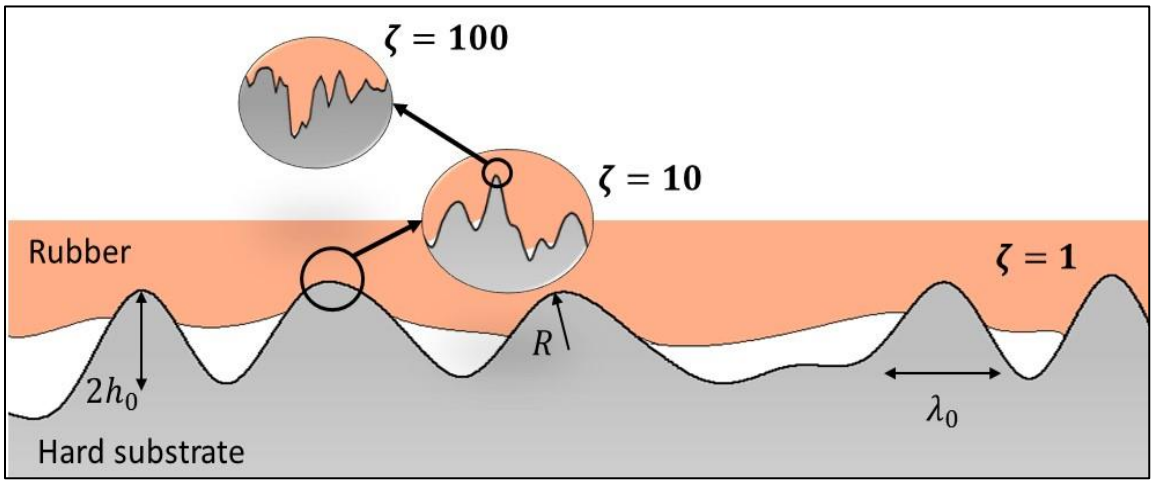


**FIGURE 3.1: SURFACE ROUGHNESS AT DIFFERENT MAGNIFICATIONS**

$$u_{z1} + u_{z2} + h = \delta \tag{3.1.}$$

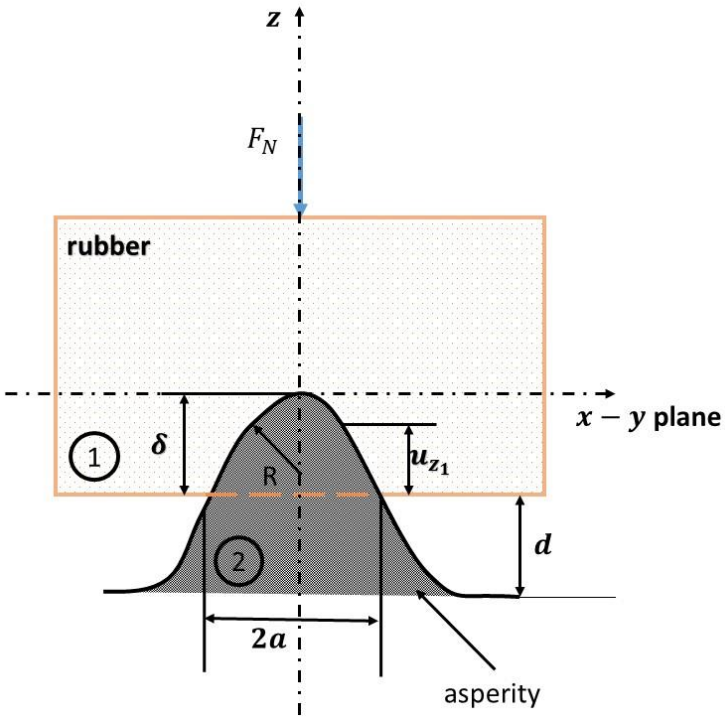


**FIGURE 3.2 HERTZ CONTACT OF PLANE SURFACE WITH SPHERICAL ASPERITY**

Where $u_{z1}\ and\ u_{z2}$ are the deformations of a point on the surface of each body respectively, $\delta$ is the approach distance at the center of the contact and h is the relative profile of the surface. In the case of a plane surface in contact with a spherical body the contact mechanics parameters for a hertz pressure distribution at the contact is given by,

Contact radius,

$$a = \pi p_0 R/2E^* \tag{3.2.}$$

Approach distance of a distant point in the center of the contact is,

$$\delta = \frac{\pi p_0 a}{2E^*} \tag{3.3.}$$

Total load on the solids is given by,

$$P = \frac{2}{3} p_0 \pi a^2 \tag{3.4.}$$

Where $p_0$the maximum amplitude of the pressure, R is the radius of the spherical elastic half space and $E^*$ is the relative modulus of both bodies given by

$$\frac{1}{E^*} = \frac{1-\nu_1^2}{E_1} + \frac{1-\nu_2^2}{E_2} \tag{3.5.}$$

If one material is considered rigid then the relative modulus of the contact is represented by a plane stress equation given by,

$$\frac{1}{E^*} = \frac{1-\nu^2}{E} \tag{3.6.}$$

**Greenwood Williamson Theory**

The previous case can be employed to contact of a plane surface with an ideal surface where the asperities are spherical with identical radius of curvature and height as

shown in Figure 3.3(A). The total load and contact area in this case will be the sum of all local loads and contact area on each asperity. However, surfaces are rough with random height distribution. In order to consider this situation Greenwood Williamson [23] considers the surface having spherical asperities with identical radius but with a height distribution. It is assumed that the contact only occurs in the summits of the asperities and the interactions of the neighboring asperities neglected.

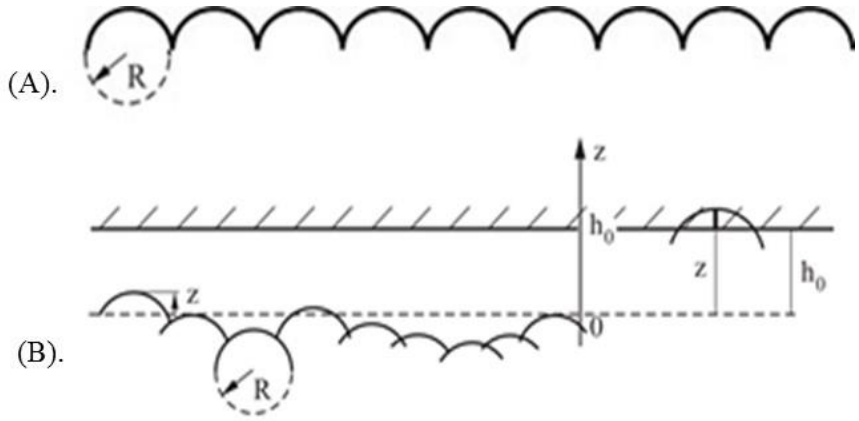


**FIGURE 3.3: (A) IDENTICAL ASPERITIES, (B) SPHERICAL ASPERITIES WITH HEIGHT DISTRIBUTION**

Probability of the number of summits in contact per unit area is given by,

$$n = N \int_{d}^{\infty} \phi_s(z)\, dz \tag{3.7.}$$

Where $N$ the total number of summit asperities, $\phi_s(z)$ the summit height distribution of the surface and $d$ the surface distance from the mean. Similar to the identical asperity case, the total contact area and the total normal load is the sum of the individuals given by Eq. (3.8, 3.9)

$$F_N = \frac{N\, R^{1/2}}{E^*} \int_{d}^{\infty} (z-d)^{3/2}\, \phi_s(z)\, dz \tag{3.8.}$$

$$A = N\pi R \int_{d}^{\infty} (z-d)\phi_s(z)dz \tag{3.9.}$$

In general form, the integrand of the Eq. (3.7-3.9) using a function called the GW function given by Eq. (3.10).

$$F_n(d) = \int_{d}^{\infty} (z-d)^n \, \phi_s(z) \, dz \tag{3.10.}$$

**Extension of Greenwood Williamson Theory**

GW theory assumes the contact to occur only at the summits and the interaction between neighboring asperities are neglected. For contact parameters governed by the large length scale asperities like the true contact stress and the mean penetration depth this approximation holds good. However, at lower length scales, the rubber tries to fill out the asperities of the surface and hence the internal contact area in the cavities apart from the external contact area must be considered as shown in Figure 3.4.

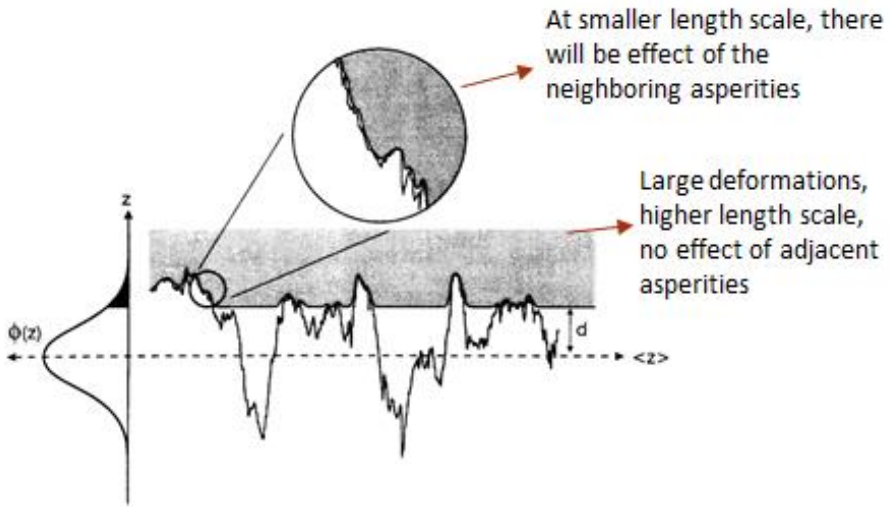


**FIGURE 3.4: MULTI SCALE DEFORMATION AT THE CONTACT INTERFACE**

In order to estimate the true contact area and the bounding frequencies, energy condition of elastic contact as a function of the length scale given by Eq. (3.11) is

applied. It states that the sum of the deformation work due to the normal force and adhesion energy should be greater than the elastic stored energy due the local deformation of rubber.

$$\sigma(\lambda)\lambda^2 h(\lambda) + \Delta\gamma\lambda h(\lambda) \gtrsim E'(\lambda)h^3(\lambda) \qquad (3.11.)$$

Where, $\lambda$ is the length scale, $h(\lambda)$ is the roughness amplitude of the surface at the particular length scale, $\Delta\gamma$ is the change in the interfacial energy given by, $\Delta\gamma = \gamma_1 + \gamma_2 - \gamma_{12}$ and $E'(\lambda)$ is the real part of the viscoelastic modulus.

## 3.2.SURFACE ROUGHNESS PARAMETERS

As discussed in the previous section all surfaces exhibit some level of roughness at certain length scales. Hence, it is very important to characterize the surface roughness for accurate predictions of contact mechanics parameters and friction especially in rubber because one of the component of rubber friction ($\mu_H$) is due to the undulations of the surface. The characterization of the surface is obtained by fractal analysis of the surface height profile. Study of surfaces using fractal analysis approach have observed most surfaces to obey self-affine behavior up to micro scale. Self-affine surfaces are statistically invariant surfaces and are isotropic in nature, i.e., the morphology of the surface is unchanged under a scale change which is given by,

$$x \to \zeta x; \quad y \to \zeta y; \quad z \to \zeta^H z$$

Where, $\zeta$ is magnification and $H$ is the Hurst exponent, which is obtained from the fractal dimension, $D_f$. Apart from the fractal dimension two length scale parameters are required to define a self-affine surface. These surface descriptors are obtained using Power Spectral Density and Height Distribution Correlation Function discussed in the next section.

## Height Difference Correlation Function (HDCF)

The height-difference correlation function predicts the mean surface height fluctuations with respect to the length scales. It is given by Eq. (3.12),

$$C_z(\lambda) = \langle (z(x+\lambda) - \langle z(x) \rangle)^2 \rangle \tag{3.12.}$$

Where, $z(x)$ is the height profile of the surface. The correlation function as a function of the length scale can be obtained for a surface as shown in Figure 3.5.

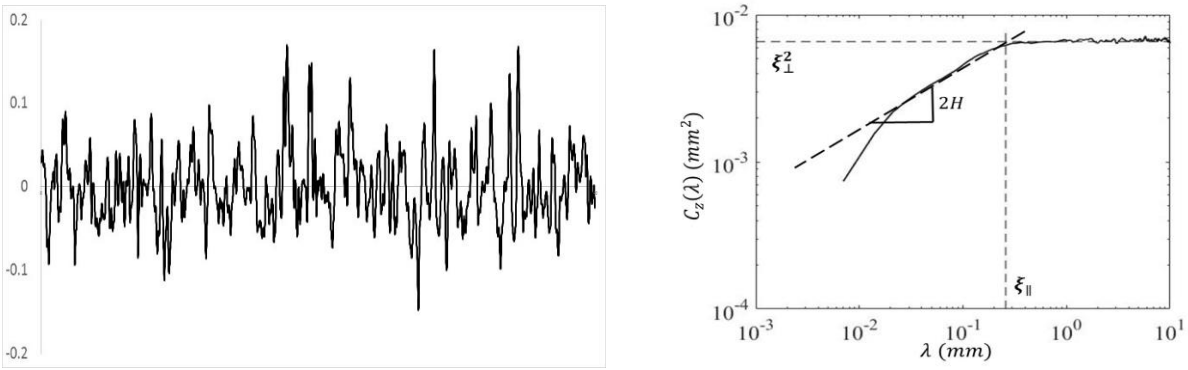


**FIGURE 3.5: HEIGHT PROFILE OF THE SURFACE WITH HEIGHT DIFFERENCE CORRELATION FUNCTION**

The slope of the correlation function will be used to predict the fractal dimension of the surface. The correlation length scales can be obtained either from the height data or by fitting the correlation function data to the Eq. (3.13) for self-affine case.

$$C_z(\lambda) = \left(\frac{\lambda}{\xi_\parallel}\right)^{2H} \xi_\perp^2 \tag{3.13.}$$

Where, $\xi_\parallel$ is the correlation length parallel to the surface or the maximum wavelength of the surface, $\xi_\perp$ is the correlation length normal to the surface or the RMS roughness amplitude of the surface, this can also be obtained from the variance of the height profile data given by the equation,

$$\xi_\perp^2 = 2\tilde{\sigma}^2 = 2\,\langle (z(x) - \langle z \rangle^2) \rangle \tag{3.14.}$$

$\xi_{\parallel}$ is also the maximum length scale below which the self-affinity of the surface is fulfilled.

**Power Spectral Density (PSD)**

This is an alternate approach to estimate the surface roughness power spectrum of the surface. It is obtained from the Fourier transform of the auto-correlation function of height-height correlation function that is given by the equation,

$$C(\boldsymbol{q}) = \frac{1}{(2\pi)^2} \int d^2x \, \langle h(\boldsymbol{x}) h(\boldsymbol{0}) \rangle e^{-i\boldsymbol{q}.\boldsymbol{x}} \tag{3.15.}$$

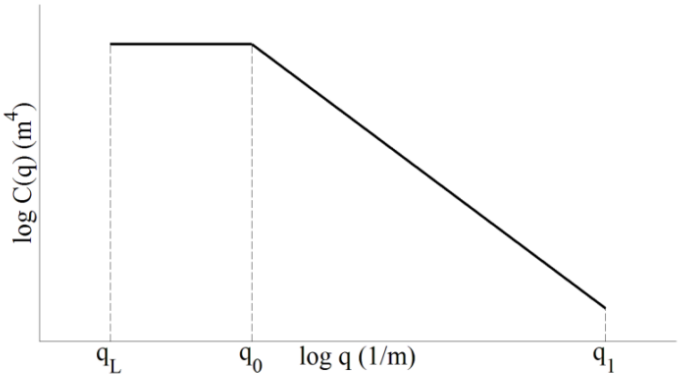


**FIGURE 3.6: POWER SPECTRAL DENSITY OF THE HEIGHT PROFILE**

Where $h(\boldsymbol{x})$ is the height profile and $\boldsymbol{x} = (x, y)$, $\langle \dots \rangle$ represents ensemble averaging over different realizations, $\boldsymbol{q} = (q_x, q_y)$ is the wave vector, but since we are considering the surface to be isotropic it only depends on $|\boldsymbol{q}|$. The surface parameters for the case of self-affine surface is obtained by considering the equation,

$$C(q) = k\left(\frac{q}{q_0}\right)^{-2(H+1)} \tag{3.16.}$$

Where $= \left(\frac{h_0}{q_0}\right)^2 \frac{H}{2\pi}$, $q_0$ is the low cut off wave vector above which the surface is self-affine. It is the inverse of the maximum wavelength given by $q_0 = 2\pi/\lambda_0$. $h_0$ is the rms roughness amplitude of the surface that is obtained using Eq. (3.17),

$$h_0 = \langle h^2 \rangle^{1/2} = \int d^2 q C(q) \tag{3.17.}$$

The fractal dimension of the surface $D_f = 3 - H$ is obtained from the slope of the curve shown in the Figure 3.6 using the relation,

$$D_f = \frac{7 + p}{2} \tag{3.18.}$$

Where $p$ is the slope of the curve in Figure 3.6.

**Height Distribution**

The height distribution of the surface is obtained either by considering the distribution as Gaussian and obtaining the probability density using Eq. (3.19) or using the experimental data.

$$\phi(z) = \frac{1}{\sqrt{2\pi\tilde{\sigma}^2}} \, e^{-\frac{(x-\mu)^2}{\tilde{\sigma}^2}} \tag{3.19.}$$

Where $\mu$ is the mean and $\tilde{\sigma}^2$ is the variance of the random variable.

The summit distribution is related to the height distribution by an affine transformation parameter that is obtained by a combination of analytical and numerical procedure. The transformed height is given by Eq. (3.20),

$$z_s = \frac{z - z_{max}}{s} + z_{max} \tag{3.20.}$$

And the new variance and mean is given by,

$$\tilde{\sigma}_s = \frac{\tilde{\sigma}}{s}$$
$$\langle z_s \rangle = z_{max}\left(1 - \frac{1}{s}\right) \tag{3.21.}$$

The summit height distribution can be given by, $\phi_s(z) = f\big(\phi(z)\big)$. It is obtained from the height distribution data by considering the values above the mean plane.

### 3.3.PERSSON'S FRICTION MODEL

This section details the physics behind the development of Persson's Friction model[29] that predict the hysteresis component of sliding friction between a rubber block and randomly rough surface. Consider a viscoelastic solid in contact with an elastic half space, the origin is taken to be at the center of the contact with $(x, y, z)$ as the coordinate system, where $z$ is normal to the surface and $(x, y)$ plane is parallel to the contact interface at $z = 0$ with $x$ as the sliding direction. The displacement field, $u_i$ of the viscoelastic solid is given by Eq. (3.22) at $z = 0$ in response to the surface stress distribution $\sigma_i = \sigma_{3i}$, which is obtained using theory of elasticity for a linear elastic isotropic medium as given in Appendix A.

$$\boldsymbol{u}(\boldsymbol{q}, \boldsymbol{\omega}) = M(\boldsymbol{q}, \boldsymbol{\omega})\boldsymbol{\sigma}(\boldsymbol{q}, \boldsymbol{\omega}) \tag{3.22.}$$

Where,

$$M = -\frac{i}{\rho c_T^2}\left(\frac{1}{S(q,\omega)}\left[Q(k,\omega)\,(\hat{z}\boldsymbol{q} - \boldsymbol{q}\hat{z}) + \left(\frac{\omega}{c_T}\right)^2 (p_L \hat{z}\hat{z} + p_T \hat{q}\hat{q})\right] + \frac{1}{p_T}\boldsymbol{e}\boldsymbol{e}\right),$$

Where, $\hat{q} = \frac{\boldsymbol{q}}{q}, \boldsymbol{e} = \hat{z} \times \hat{q}$

$$Q = 2q^2 - \frac{\omega^2}{c_T^2} + 2p_T\, p_L; \qquad S = \left(\frac{\omega^2}{c_T^2} - 2q^2\right)^2 + 4q^2 p_T p_L$$

Assuming stationary sliding at the contact interface, the deformations due to the surface stresses acting only in the z-direction and neglecting the deformations in all directions except the normal direction,

$$u_z(\boldsymbol{q},\omega) = M_{zz}(\boldsymbol{q},\omega)\sigma_z(\boldsymbol{q},\omega) \tag{3.23.}$$

Where, $(M_{zz})^{-1} = -\frac{E(\omega)q}{2(1-\nu^2)}$ if stresses are given. If the displacements are specified then $(M_{zz})^{-1} = -\frac{2\,Eq(1-\nu)}{(1+\nu)(3-4\nu)}$

The Fourier transform of the displacement field is given by,

$$\boldsymbol{u}(q,\omega) = \frac{1}{(2\pi)^3}\int d^2x\, dt\, \boldsymbol{u}(\boldsymbol{x},t)e^{-i(\boldsymbol{q}.\boldsymbol{x}-\omega t)} \tag{3.24.}$$

Considering,

$$\boldsymbol{u}(\boldsymbol{x},t) = \boldsymbol{u}(\boldsymbol{x}-\boldsymbol{v}t) \tag{3.25.}$$

Then,

$$\boldsymbol{u}(\boldsymbol{q},\omega) = \delta(\omega-\boldsymbol{q}.\boldsymbol{v})\,\boldsymbol{u}(\boldsymbol{q}) \tag{3.26.}$$

The energy dissipated due to the oscillations of the displacement field during the sliding of the viscoelastic medium on a surface is given by Eq. (3.27),

$$\Delta E = \int d^2x dt\, \dot{u}.\sigma \tag{3.27.}$$

Fourier transformation of the equation and substituting the constitutive relation given by Eq. (3.22) gives,

$$\Delta E = (2\pi)^2 t_0 \int d^2q(-i\omega)[M_{zz}(-\boldsymbol{q},-\omega)]^{-1}\, u_z(\boldsymbol{q})u_z(-\boldsymbol{q}) \tag{3.28.}$$

The energy dissipated at the contact can also be represented by the frictional shear stress using Eq. (3.29),

$$\Delta E = \sigma_f A_0 v T \tag{3.29.}$$

Hence, the frictional shear stress obtained from Eq. (3.28 & 3.29) is given by,

$$\sigma_f = \frac{(2\pi)^2}{A_0 v} \int d^2q(-i\omega)[M_{zz}(-\boldsymbol{q}, -\omega)]^{-1} \langle u_z(\boldsymbol{q}) u_z(-\boldsymbol{q}) \rangle \tag{3.30.}$$

Since the frictional sliding is only considered in the longitudinal direction, the energy dissipation is only due to the undulations in the x-direction. Thus, $\omega = q_x v$, where considering polar coordinates, $q_x = q\ cos\ \phi$. Also, it is assumed that the rubber deforms completely to follow the substrates surface profile, $u_z \approx h(x)$. Hence, considering these, the Eq. (3.30) reduces to,

$$\sigma_f = \frac{(2\pi)^2}{A_0} \int d^2q q_x [M_{zz}(-\boldsymbol{q}, -q_x v)]^{-1} \langle h(\boldsymbol{q}) h(-\boldsymbol{q}) \rangle \tag{3.31.}$$

Substituting $(M_{zz})^{-1} = -\frac{E(\omega)q}{2(1-\nu^2)}$ and noting,

$$\langle h(q)h(-q) \rangle = \frac{A_0}{(2\pi)^2}\ C(q)$$

$$\sigma_f = \frac{1}{2} \int d^2q\ q^2 \cos\phi\ C(q)\ Im \frac{E(qv cos\ \phi)}{1-\nu^2} \tag{3.32.}$$

The friction coefficient can be obtained from the general friction relationship given by Eq. (2.1)

$$\begin{aligned} \mu &= \frac{F_f}{F_N} = \frac{\sigma_f A(\boldsymbol{q})}{\sigma_0 A_0} = \frac{\sigma_f}{\sigma_0}\ P(\boldsymbol{q}) \\ \mu &= \frac{1}{2} \int d^2q\ q^2 \cos\phi\ P(\boldsymbol{q}) C(\boldsymbol{q})\ Im \frac{E(qv cos\ \phi)}{(1-\nu^2)\sigma_0} \end{aligned} \tag{3.33.}$$

Considering the surface to be isotropic $C(\boldsymbol{q})$ and $P(\boldsymbol{q})$ only depend on the $|\boldsymbol{q}|$, Eq. (3.33) reduces to,

$$\mu = \frac{1}{2}\int dq\, q^3 P(q) C(q) \int_0^{2\pi} d\phi\, \cos\phi\; Im \frac{E(qv\cos\phi)}{(1-\nu^2)\sigma_0} \qquad (3.34.)$$

**Contact mechanics theory – Area Ratio $\left(\boldsymbol{P}(\boldsymbol{q})\right)$**

Persson develops a contact theory to obtain the area ratio required to predict the friction coefficient in the true contact area. He considers a uniform pressure distribution ($\sigma(x) = \sigma_0$) at the surface contact for a magnification of $\zeta = 1$.

Persson develops a contact theory by considering the stress probability distribution at the contact interface. The total load acting on the elastic medium can be denoted by Eq. (3.35),

$$F_N = \sigma_0 A_0 = \langle\sigma\rangle_\zeta\, P(\zeta) A_0 \qquad (3.35.)$$

Where $\langle\sigma\rangle_\zeta$ is the average pressure in the contact area at the length scale, $\lambda = L/\zeta$. Hence,

$$P(\zeta) = \frac{\sigma_0}{\langle\sigma\rangle_\zeta}$$

The average pressure at a length scale $\zeta$ can be denoted by the stress probability distribution $p(\sigma, \zeta)$ using the Eq. (3.36)

$$\langle\sigma\rangle_\zeta = \frac{\int d\sigma\, \sigma\, p(\sigma,\zeta)}{\int d\sigma\, p(\sigma,\zeta)} \qquad (3.36.)$$

As per the property of probability distribution, the numerator of the above equation represents the mean value of the stress or the average pressure hence,

$$\int d\sigma\, \sigma\, p(\sigma,\zeta) = \sigma_0 \qquad (3.37.)$$

Considering the relation for the stress probability distribution a diffusion relation is obtained for the stress probability distribution is obtained with respect to magnification and stress which is solved using the respective boundary condition and initial condition as given in Appendix B, we arrive at,

$$P(\zeta) = \frac{2}{\pi}\int_0^{\infty} dx' \frac{\sin x'}{x'} \exp\left[-x'^2 \int_1^{\zeta} d\zeta' g(\zeta')\right]; \quad x' = \frac{n\pi\sigma_0}{\sigma_y} \qquad (3.38.)$$

Where,

$$g(\zeta) = \frac{1}{8} q_L q^3 C(q) \int_0^{2\pi} d\phi \ \frac{|E(qv\cos\phi)|}{(1-\nu^2)\sigma_0^2}$$

In general tire application, the average pressure at the contact will be in the rage of $0.2 - 0.8\,MPa$ which is far less than the yield strength of rubber, $\sigma_0 \ll E(0)$. Assuming uniform pressure distribution at the contact, we can approximate $\sin x \approx x$. Hence, the area ratio reduces to,

$$P(q) = [\pi G(q)]^{-\frac{1}{2}} \qquad (3.39.)$$

Where, $G(q) = \frac{1}{8} q_L \int_{q_0}^{q_1} q^3 C(q) \int_0^{2\pi} d\phi \ \frac{|E(qv\cos\phi)|}{(1-\nu^2)\sigma_0^2}$

Taking into account the condition, $P(q) \to 1$ when $G(q) \to 0$, using interpolation we get,

$$P(q) = \left(1 + [\pi G(q)]^{\frac{3}{2}}\right)^{-1/3} \qquad (3.40.)$$

**Including Frictional heating and flash temperature**

The frictional shear stresses generated at the contact interface will lead to energy dissipation at the contact at different length scales as given by Figure 3.7. At low sliding velocities, this is diffused inside the rubber and there is no temperature rise.

However, at higher velocities ($> 10^{-2} m/s$) there is no time for the energy to be diffused into the rubber and will result in increase of the surface temperature also called the flash temperature. This increase in the temperature will affect the material properties and alters the friction coefficient. The heat diffusion relation as given by Eq. (3.41) can be used to determine this temperature rise,

$$\frac{\partial T}{\partial t} - D\nabla^2 T = \frac{\dot{Q}(z,t)}{\rho C_v} \tag{3.41.}$$

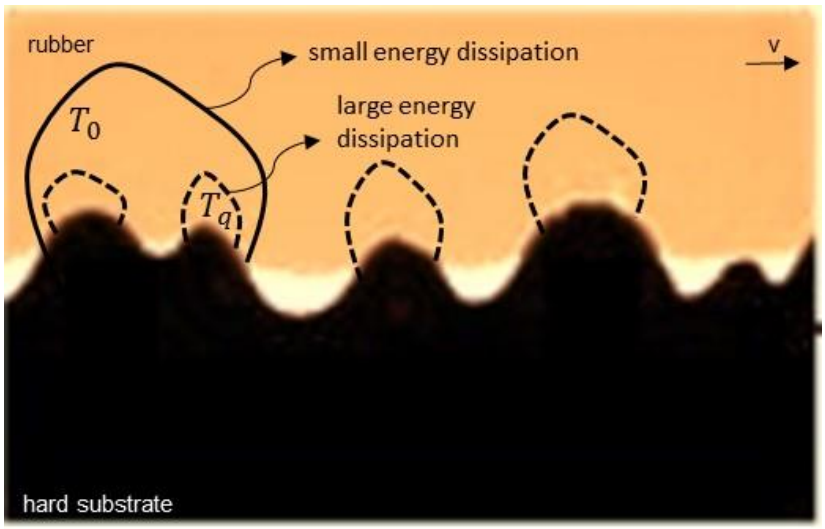


**FIGURE 3.7: ENERGY DISSIPATED AT MULTIPLE LENGTH SCALES**

Where $D = \lambda_k / \rho C_V$ is the heat diffusivity and $\dot{Q}$ is the amount of energy generated per unit volume per unit time due to the average frictional shear stress at a macro asperity contact. $\rho$ is the mass density, $\lambda_k$ is the thermal conductivity and $C_V$ is the specific heat. The heat generation is due to the frictional shear stresses given by Eq. (3.42),

$$\dot{Q}(z,t) = \frac{\sigma_f v}{\lambda} \tag{3.42.}$$

Assuming stationary sliding, no heat diffusion from the rubber to the substrate and neglecting the energy due to adhesion friction the boundary and initial conditions given by,

$$T(z,0) = T_0 \quad --Initial\ Condition$$
$$T(L,t) = T_0;\ \frac{\partial T}{\partial z}(z=0) = 0 \quad --Boundary\ condition \tag{3.43.}$$

$T_0$ is the background temperature. Applying the initial and boundary condition and solving Eq. (3.41) we obtain the temperature at different length scales,

$$T_q = T_0 + \int_0^\infty dq' g(q,q') f(q') \tag{3.44.}$$

Where,

$$f(q) = \frac{vq^4}{\rho C_v} C(q) \frac{P(q)}{P(q_m)} \int d\phi \cos\phi\ Im \frac{E\left(qvcos\ \phi, T_q\right)}{1-\nu^2}$$

$$g(q,q') = \frac{1}{\pi}\int_0^\infty dk \frac{1}{Dk^2}\left(1 - e^{-Dk^2 t_0}\right)\frac{4q'}{k^2+4q'^2}\frac{4q^2}{k^2+4q^2}$$

Here, $f(q)$ is the heat generation term and $g(q,q')$ is the heat diffusion term. In order to determine the flash temperature at different length scales, Eq. (3.44) are solved iteratively by considering initial guesses that depends on the background temperature. The WLF shift factor is used to determine the temperature dependent material properties. It is given by Eq. (3.45),

$$\log_{10} a_T = -\frac{C_1(T-T_0)}{C_2 + T - T_0}$$
$$E(\omega, T) = E(a_T\omega, T_0) \tag{3.45.}$$

Where, $C_1$ and $C_2$ are empirical constants determined from DMA experiments. After estimating the temperature at different length scale, the corresponding friction coefficient for a self-affine surface is determined using Eq. (3.46) and considering the temperature dependent material properties.

$$\mu_{hys}(v_s, q, T_q) = \frac{1}{2}\int_{q_0}^{q_1} dq\, q^3\, C(q)P(q) \int_0^{2\pi} d\phi \cos\phi\, Im \frac{E\left(qv_s\, cos\, \phi, T_q\right)}{(1-\nu^2)\sigma_0} \tag{3.46.}$$

$$P\left(q, T_q\right) \approx \left(1 + \left[\frac{\pi}{8}\int_{q_L}^{q} dq\, q^3 C(q) \int_0^{2\pi} d\phi \left|\frac{E(qv_s\, cos\phi,\ T_q)}{(1-\nu^2)\sigma_0}\right|^2\right]^{3/2}\right)^{-1/3}$$

### 3.4.KLUPPEL'S MODEL

Kluppel follows a similar energy based approach to obtain the friction coefficient where the energy dissipated due to the deformations of the surface is given by the Eq. (3.47).

$$\Delta E = \int_0^V \int_0^t d^3x\, dt\, \boldsymbol{\sigma}.\dot{\boldsymbol{\varepsilon}} \tag{3.47.}$$

The same coordinate system as that of Persson's friction model is considered. However, in this case Kluppel assumes uniaxial deformations. The Fourier transform of stress and strain to the frequency domain is considered given by Eq. (3.48) and the energy dissipated is transformed to frequency domain as given by Eq. (3.49)

$$\sigma(t) = \int d\omega\, \sigma(\omega) e^{i\omega t}$$
$$\varepsilon(t) = \int d\omega\, \varepsilon^*(\omega)\, e^{i\omega t} \tag{3.48.}$$

$$\Delta E = \frac{V}{2\pi}\int d\omega\, (-i\omega)\, \sigma(\omega)\, \varepsilon^*(\omega) \tag{3.49.}$$

Considering Hooke's law ($\sigma(\omega) = E(\omega)\,\hat{\varepsilon}(\omega)$) for the stress-strain relation in the frequency domain the energy dissipated for the macroscale in the contact interface simplifies to,

$$\langle \Delta E \rangle = \frac{V}{2\pi}\, Im\left[\int d\omega\; \omega\; E(\omega) \int d\omega' \delta(\omega - \omega')\, \langle \hat{\varepsilon}(\omega)\varepsilon^*(\omega')\rangle\right] \quad (3.50.)$$

Considering the deformations to follow the surface profile of the substrate the energy dissipation reduces to,

$$\langle \Delta E \rangle = \frac{V}{2(2\pi)^2} t_0 \int d\omega\; \omega\; E"(\omega)\, S(\omega) \quad (3.51.)$$

Where $E"(\omega)$ is the loss modulus of rubber, $S(\omega)$ is the power spectral density of the surface, $V = \langle \delta \rangle\, A_0$ is the volume of the excited layer. Relating this to energy dissipated from the frictional shear stress gives the hysteresis friction coefficient as an integral over excitation frequency interval $[\omega_{min}, \omega_{max}]$,

$$\mu_H = \frac{F_f}{F_N} = \frac{1}{2(2\pi)^2}\, \frac{\langle \delta \rangle}{\sigma_0\, v} \int_{\omega_{min}}^{\omega_{max}} d\omega\; \omega\; E"(\omega)\, S(\omega) \quad (3.52.)$$

Where $\langle \delta \rangle$ is the excited layer thickness of rubber which is approximated to the mean penetration depth, $\langle z_p \rangle$ ($\langle \delta \rangle \approx \langle z_p \rangle$). By considering the surface roughness to be self-affine, the power spectral density is obtained from the surface descriptors using HDCF (Section 3.2) and is given by,

$$S(\omega) = \frac{H \xi_\perp^2}{2\pi v \xi_\parallel} \left(\frac{\omega}{\omega_{min}}\right)^{-(7-2D_f)} \quad (3.53.)$$

Kluppel uses the contact mechanics theory developed by the Greenwood Williamson to obtain the macro scale parameters like the mean penetration depth and true contact stress given by Eq. (3.54),

$$\langle z_p \rangle = \tilde{\sigma}\, F_1\left(\frac{d}{\tilde{\sigma}}\right)$$
$$\sigma_0' = \frac{16}{9} E'(\omega_{min}) R^{\frac{1}{2}} N_s \tilde{\sigma_s} F_{\frac{3}{2}}\left(\frac{d}{\tilde{\sigma_s}}\right) \tag{3.54.}$$

Where macro asperity radius of curvature is $R = \frac{\xi_{\parallel}^2}{4\pi^2 \xi_{\perp}}$, $N_s = \xi_{\parallel}^{-2}$ is the total number of summits, $d$ is the separation of the surface, $\tilde{\sigma_s}$ is the standard deviation of the summit heights and $F_n(t)$ is the GW function. The separation distance between the surfaces is obtained from the hertz contact theory Eq. (3.55),

$$d = \xi_{\perp} - \frac{\pi^2 \sigma_0^2 R}{4|E(\omega_{min})|^2} \tag{3.55.}$$

In the frequency interval, the minimum frequency $\omega_{min} = 2\pi/\xi_{\parallel}$ depends on the maximum length scale and the maximum frequency is related the minimum length scale. GW theory assumes that the contact only occurs at the summits of the asperities, but at higher magnifications, the rubber tends to fill into the cavities that effects minimum length scale and also the true area of contact. In order to consider this, Kluppel considers an extension to this theory where he considers an energy condition for elastic contact as given by Eq. (3.11) to obtain the minimum length scale as a function of the sliding velocity and the load given by Eq. (3.56),

$$\lambda_{min} = \xi_{\parallel} \left( \frac{0.09\pi s^{\frac{3}{2}} \xi_{\perp} (2D-4) |E(\lambda_{min})| F_0\left(\frac{d}{\tilde{\sigma}}\right)}{\xi_{\parallel}(2D-2)\left|E(\xi_{\parallel})\right| F_{3/2}\left(\frac{d_s}{\tilde{\sigma_s}}\right)} \right)^{\frac{1}{3D-6}} \tag{3.56.}$$

The above equation is an implicit equation in $\lambda_{min}$ and solved iteratively. The true area of contact using a yard stick or box counting method [27] is considered for the case of a self-affine surface which is found to agree a power law relation given by Eq. (3.57),

$$A_c(\lambda) = A_{c,0}\left(\frac{\lambda}{\xi_{\parallel}}\right)^{2-D} \quad (3.57.)$$

## 3.5.THEORETICAL COMPARISON OF BOTH THE MODELS:

Persson and Kluppel focused on developing a friction model that can predict the hysteretic friction coefficient based on the internal energy dissipated due to the elastic deformations from the undulations of the surface. The friction model obtained is a function of viscoelastic modulus, surface roughness parameters and sliding velocity. Fourier transformations performed to solve for the friction coefficient. The theoretical variation of the models are:

- Kluppel considers the deformation at the surface to be uniaxial and considers a Hooke's law to obtain the constitutive relation in the frequency domain. On the other hand, Persson obtains the constitutive relation by considering the balance laws of theory of elasticity for a linear isotropic material (continuity, conservation of momentum and energy) for a uniform pressure distribution at the interface and then solving by decomposition of the displacement field [30] (see Appendix A).
- Kluppel model is applicable to be self-affine surfaces (statistically invariant surfaces) that is characterized using HDCF. However, Persson uses the surface roughness power spectrum approach to characterize the surface roughness and further accounts for randomly rough surfaces (see section 3.2).
- Kluppel's uses an extension of the Greenwood Williamson contact theory at which he uses the GW theory to obtain the macroscale parameters like the mean penetration depth and normal load distribution. He extends this contact theory to account for the perturbations due to the neighboring asperities in the micro scale by obtaining the minimum length scale using an energy condition for elastic contact (Eq. 3.11), where he separates the normal regime and

adhesion regime. Kluppel's model and also accounts for the load dependency in both adhesion and hysteresis by obtaining the true contact area and the minimum coupling length scale as a function of the normal load through the surface distance

- On the other hand, Persson develops his own contact theory by considering the stress probability distribution at the contact interface as a function of length scale and stress acting in that length scale. He obtains a diffusion relation for the stress probability distribution that is then solved to obtain true contact area. However, Persson in this process assumes that there is uniform pressure distribution and also considers the rubber to follow surface profile and will have complete contact with the surface. This approach eliminates the dependency of the load or normal pressure on friction coefficient. In later research [31] this has been corrected using a correction factor, the value of which is obtained by comparing with experimental or molecular dynamics simulations.

These variation makes the theories unique, for example Kluppel considers both micro and macro scale to obtain the friction coefficient [32]. Persson obtains the friction coefficient by considering only single regime.

# 4. EXPERIMENTAL DATA

In this section, we detail the experimental data required for the simulation of the model and how to obtain it. The surface roughness profile required for characterization of the surface is obtained using Nanovea Profilometer. Material properties are obtained using the Dynamical Mechanical Analysis and finally, the experimental friction coefficient required for the validation of the model is obtained using the Dynamic friction tester.

## 4.1.SURFACE HEIGHT PROFILE

Nanovea Jr25 is a Non-Contact Profilometer used to obtain the height profile of the surface to predict the surface characteristics as shown in Figure 4.1. The measurement is based on Chromatic Confocal optical technology and utilizes the concept of raster scan. A white light emitted with high degree of chromatic aberration through a series of lenses from the optical pen. The light is reflected back into the optical pen through a pin hole filter which allows only the measurement range frequency which is set based on the surface. The light then passes through a spectrometer at which based on the set calibration the wavelength will correspond to a specific distance at that point. The instrument can measure a maximum surface area of $50 \times 50\ mm$ and has a resolution of 7 $\mu m$ in $x$ and $y$ direction.

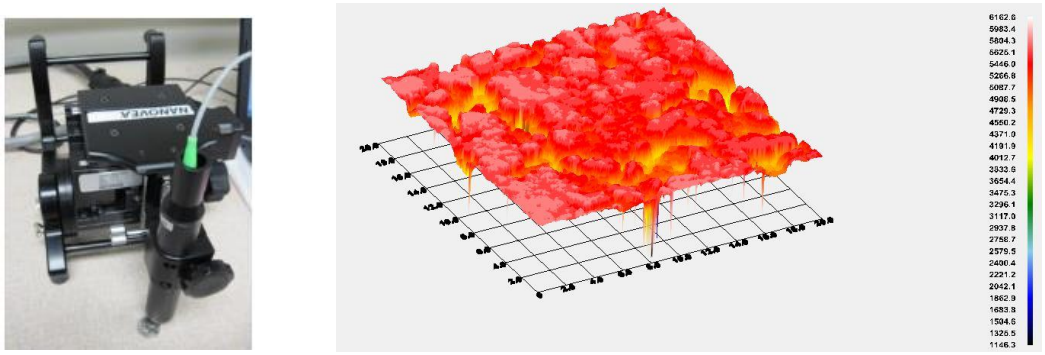

**FIGURE 4.1: NANOVEA PROFILOMETER WITH 3D HEIGHT PROFILE OF ASPHALT TRACK**

The height profile of a 120 grit and asphalt surface is measured over a contact length of $40mm$ with a resolution $7\mu m$ as shown in Figure 4.2. The profile thus measured is passed through a Split cosine bell window (SCBW) [20] to remove the jumps in the edges of the signal which will affect the power spectrum. Any slope of the surface during the measurement is removed by calculating the surface slope and correcting the sample data accordingly using the Eq. (4.1),

$$b_1 = \frac{12\sum_{i=1}^{N-1} i\, z_i - 6(N-1)\sum_{i=0}^{N-1} z_i}{N(N+1)(N-1)}$$
$$Z_i = z_i - b_1 i \qquad (4.1.)$$

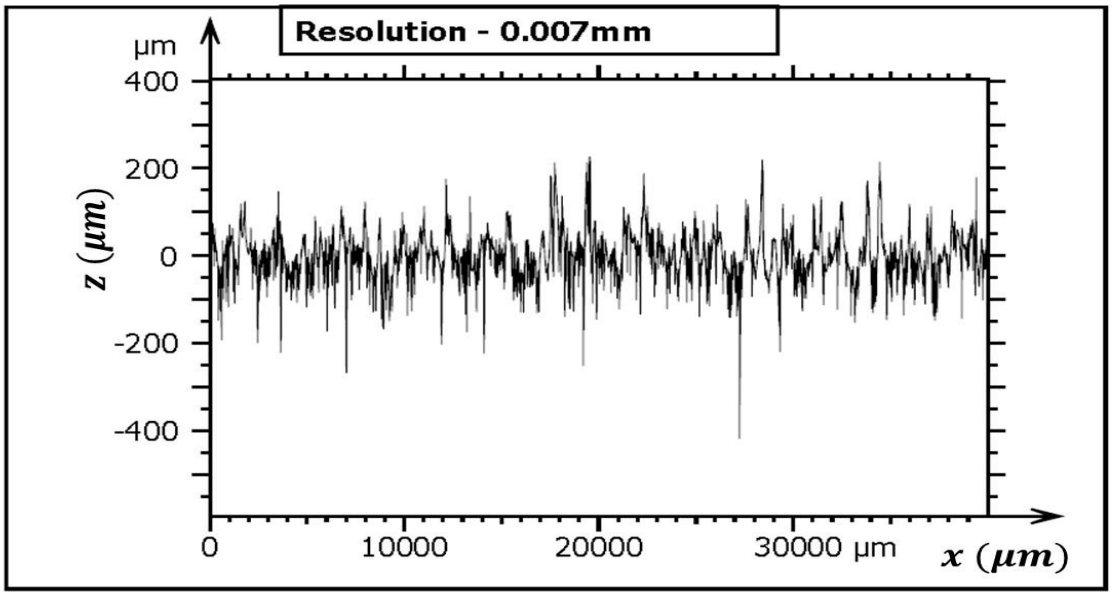


**FIGURE 4.2: LINE PROFILE OF 120-GRIT SURFACE WITH RESOLUTION $7\mu m$**

Where N is the number of data points, $z_i$ is the measured height data with surface slope. The surface is then offset to set the mean of the surface, $\langle z(x)\rangle = 0$.

## 4.2.DYNAMICAL MECHANICAL ANALYSIS

The frequency dependent complex elastic modulus of Compound A is obtained using a Dynamic Mechanical Analysis (DMA). DMA is a method used to

characterize the dynamic material properties especially for viscoelastic materials. A sinusoidal strain amplitude is applied to the material under specific background temperature at varying frequency range (depending on the instrumentation and material) and stress is measured as the output. The stress – strain response and the lag between them is used to obtain the complex modulus of the material. The DMA is repeated for different temperature for obtaining the dynamic moduli of the material for a wide range of frequency using Time Temperature Superposition.

DMA of Compound A is performed for a frequency range of $1\ Hz - \ 35\ Hz$ and for temperature range in between $-50^oC - 120^oC$ with steps of $5^oC$. The elastic modulus thus obtained for a low strain amplitude is shown in Figure 4.3. The Time temperature superposition is given in section 5.1.

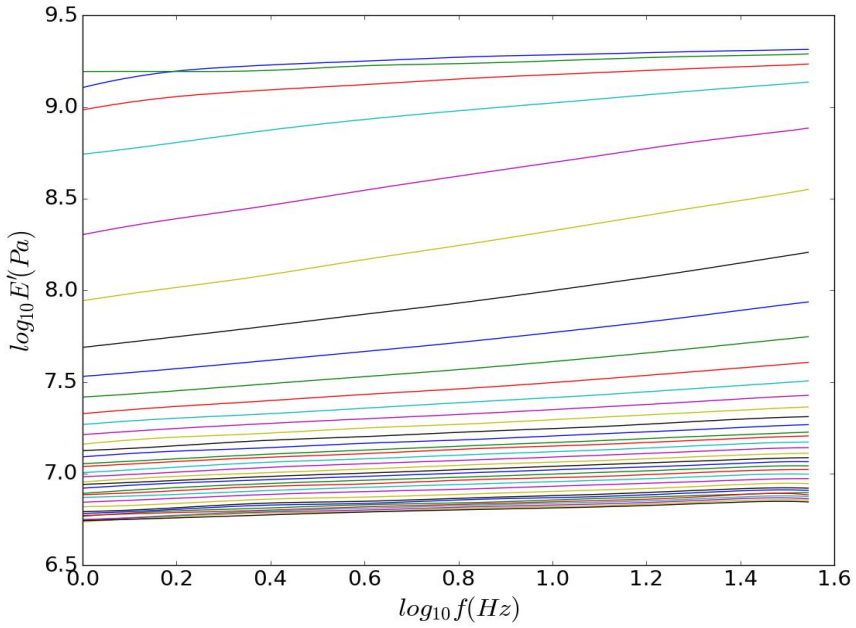


**FIGURE 4.3: DMA DATA OF RUBBER COMPOUND**

## 4.3.EXPERIMENTAL FRICTION USING DYNAMIC FRICTION TESTER:

Dynamic Friction tester is used to obtain the experimental friction as a function of sliding velocity and load for Compound A on a 120-grit surface. The friction tester is capable of running the experiments under controlled normal load and longitudinal velocities. The frictional and normal force acting on the sample is measured using the load cells attached in the longitudinal and normal direction as shown in Figure 4.4. The longitudinal sliding velocity of the sample is set by varying the angular velocity of sample and disk. Experiments was run for a Compound A sliding on a 120 grit surface for a nominal pressure of $0.4MPa$ at 5 different sliding velocities and the results are as shown in Figure 4.5. The experiments were repeated at different loads and the results are shown in Figure 4.5.

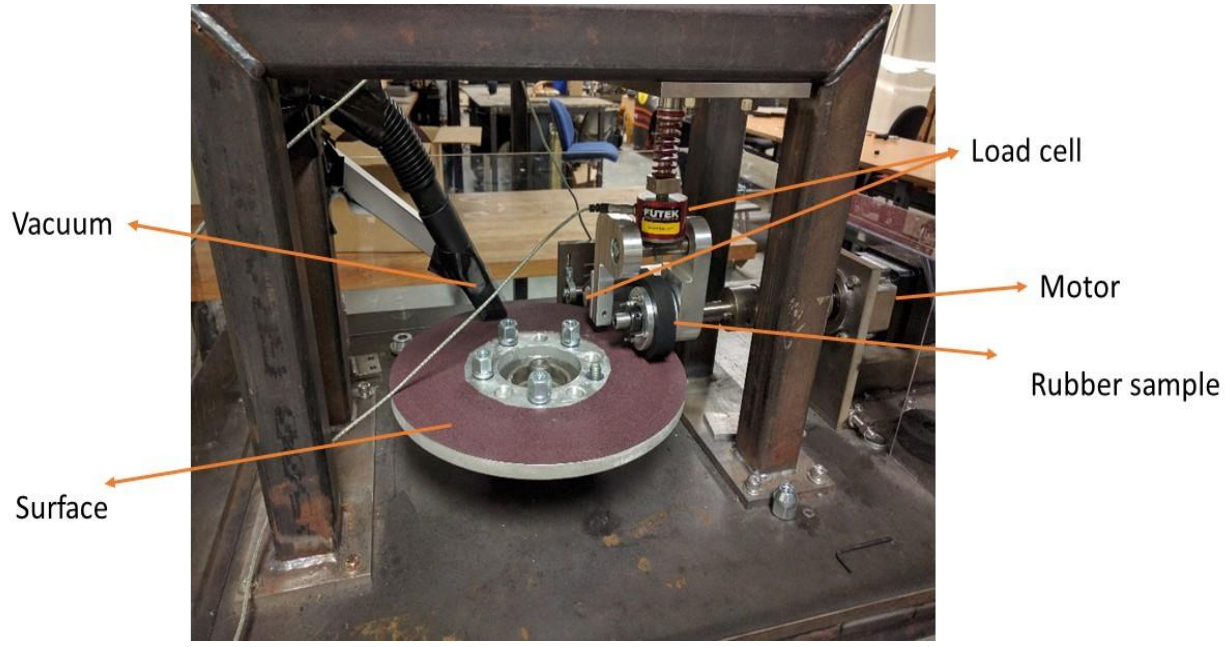


**FIGURE 4.4: DYNAMIC FRICTION TESTER**

(A).

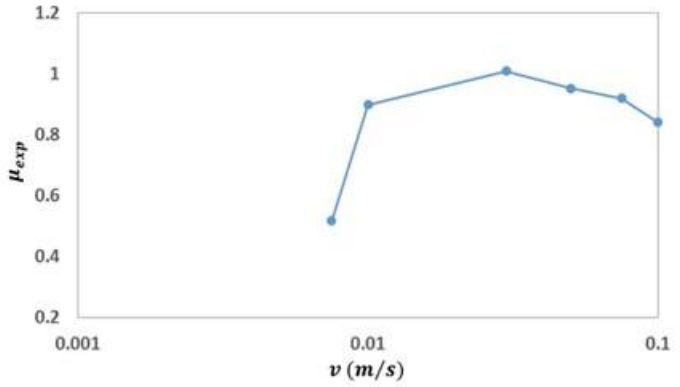


(B).

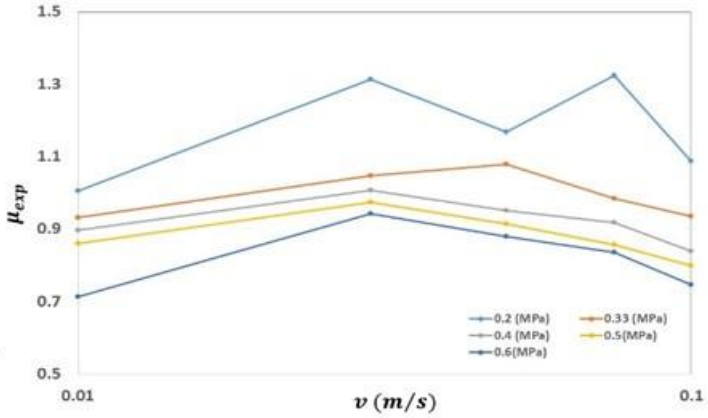


**FIGURE 4.5: FRICTION DATA FROM DYNAMIC FRICTION TESTER. (A) AT NORMAL PRESSURE $0.4MPa$, (B) AT DIFFERENT NORMAL PRESSURES**

# 5. MODEL RESULTS AND DISCUSSION

In this chapter, the simulation results for equations discussed in chapter 3 are solved for different operating conditions. We will start with a discussion on how to obtain the input parameters for the different model from the experimental data in the previous chapter. After that validation and comparison of the models under different conditions are discussed along with validation of the model with experimental results obtained using Dynamic Friction Tester.

## 5.1. INPUT PARAMETERS

The main input parameters required to obtain the friction coefficient are the material properties, surface descriptors and the operating conditions. The operating conditions for a block sliding on a surface are the normal load $(F_N)$ or pressure $(\sigma_0)$ and the sliding velocity$(v)$.

### Master curve of the Material

As discussed previously the complex modulus of the viscoelastic material at different frequencies and temperature is obtained using the DMA analysis. However, due to time and machine restrictions the analysis can only be performed in a certain range of frequencies mainly in between 1-100 Hz depending on the shape and size of specimen. In order to observe the behavior of the polymer at short and long time periods an extrapolation technique known as the Time temperature superposition is used. This technique is based on the principle that time and temperature dependence can be correlated using a shift factor, i.e., the behavior of the material at lower temperature is analogous to its behavior at higher frequencies and vice versa.

One such superposition principle [10] will be used here to obtain the master curve from the DMA data of Compound A where we consider that the elastic modulus at

different temperature from DMA, which is transformed with respect to a reference temperature using a horizontal shift factor $(a_T)$,

$$E'(\omega, T) = E'(a_T\omega, T_0) \tag{5.1}$$

$$a_T = \frac{\omega_T}{\omega_0} \tag{5.2}$$

Considering the logarithmic scale for the modulus and frequency we get,

$$\log E'(\log \omega\,, T) = \log E'(\log a_T + \log \omega\,, T_0) \tag{5.3}$$

Hence, if we obtain the distance of the modulus curve as a function of frequency in a log-log scale at different temperatures with respect to a reference temperature we can obtain the master curve. This distance is calculated by using the following approach,

- From the DMA test data, the curves of any of the viscoelastic property ($E'$ is selected in general) is obtained at different frequencies and temperature and plotted in a log-log scale
- A smooth curve of the viscoelastic property is obtained by fitting the data to a b-spline curve as shown in Figure 5.1.

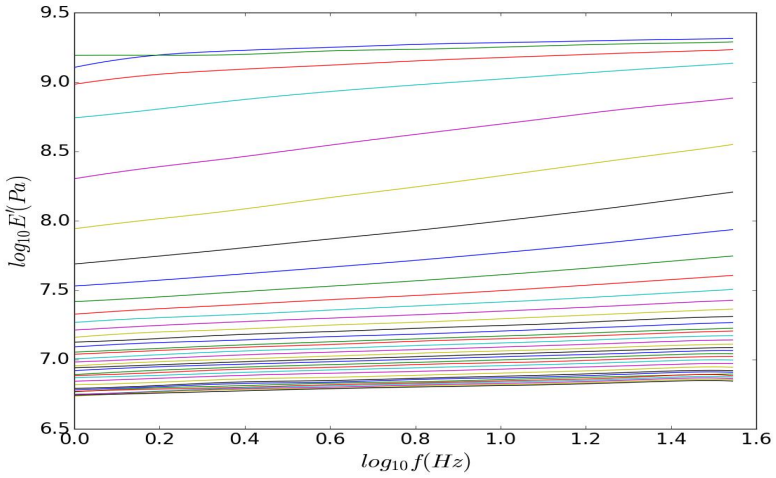


**FIGURE 5.1: DMA DATA OF RUBBER COMPOUND**

- The common range of the viscoelastic property is selected for the two adjacent temperature curves and the average horizontal distance between them is obtained by calculating the difference in frequencies in log scale as shown in Figure 5.2.

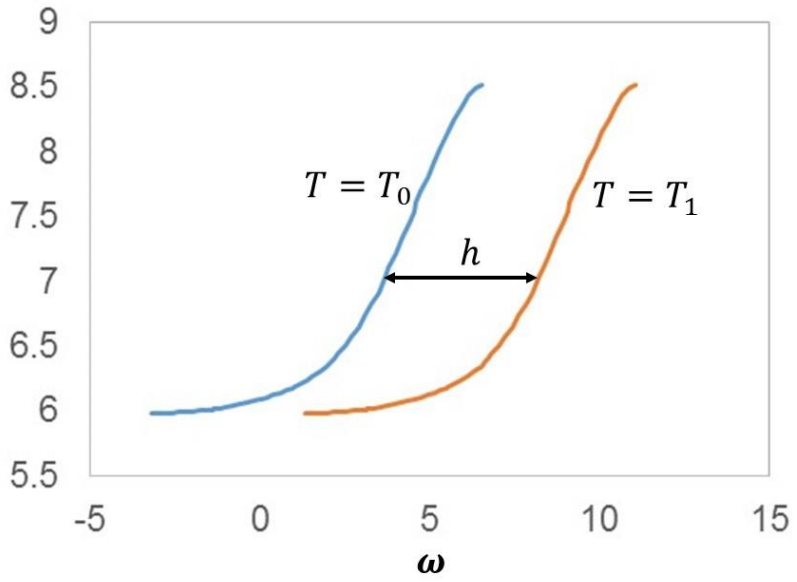


**FIGURE 5.2: HORIZONTAL SHIFT CALCULATION**

- The reference temperature is selected based on the glass transition temperature and the cumulative distance between the curve at reference temperature and the curve at different temperature is obtained which is the shift factor $(a_T)$ in the log scale for different frequencies as shown in Figure 5.3

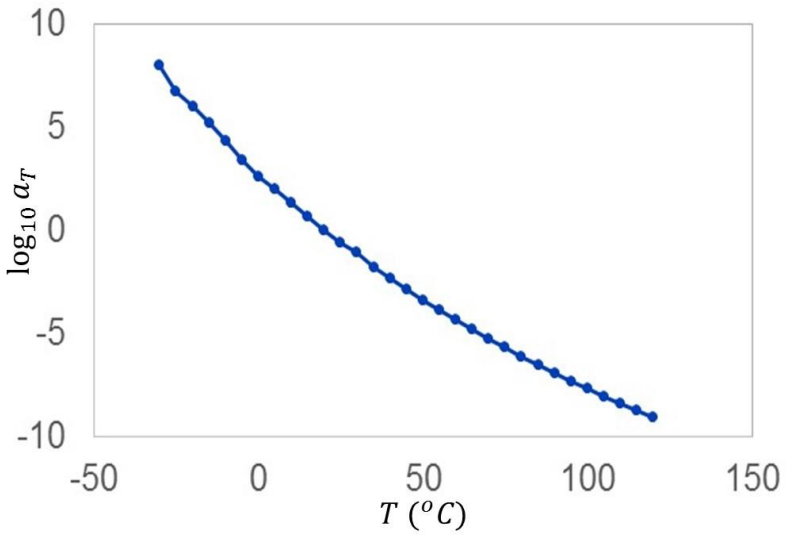


**FIGURE 5.3: SHIFT FACTOR AS A FUNCTION OF TEMPERATURE**

- The master curve is then obtained by shifting the frequencies of the viscoelastic property curves by the shift factor as shown in Figure 5.4.

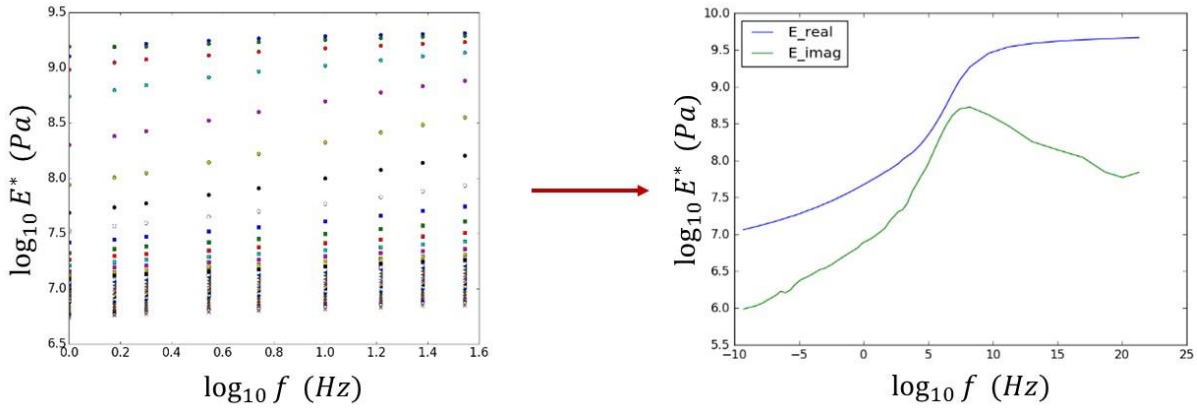


**FIGURE 5.4: MASTER CURVE FOR THE RUBBER COMPOUND**

*Temperature dependence:*

In order to obtain the complex modulus as a function of the temperature or to predict the master curve at different temperature the same TTS principle can be used and shift factor can be used to shift the properties to other temperature. Empirical or semi

empirical relations can be used to obtain the horizontal shift factor to relate the temperature dependence. Two most important are the Arrhenius and the WLF (William–Landel–Ferry) equation which is given by,

$$WLF\ Equation:\ \log a_T = -\frac{C_1(T - T_0)}{C_2 + (T - T_0)} \tag{5.4}$$

Where $C_1$ and $C_2$ are the material coefficient which is obtained by fitting the experimentally obtained shift factor to the above WLF equation. $T_0$ is the reference temperature with respect to which the shift factor vs temperature curve is obtained. As we can see from the equation $C_1$ is dimensionless but $C_2$ has units of temperature.

$$Arhennius\ Equation: \log a_T = \frac{E_a}{R}\left(\frac{1}{T} - \frac{1}{T_0}\right) \tag{5.5}$$

Where, $E_a$ is the activation energy and $R$ is the universal gas constant. The Arrhenius equation is mainly used for temperature below the glass transition temperature and at moderate temperature up to $100^oC$ above the glass transition temperature; we can use the WLF equation to obtain the viscoelastic properties.

We use the WLF equation to obtain the shift factor at different temperature. The experimental shift factor curve is fitted to the WLF equation and the material coefficient are found to be $C_1 = 32$ and $C_2 = 259\,K$ for a reference temperature $T_0 = 20\ C$.

*Large strain Modulus:*

In the case of rubber sliding on a rigid contact surface, the strain rates observed at the contact is very large, approx. 100%. However, the DMA data is obtained at low strains in the range of 0.01% to 3% due to the operating range of machine, as it is very hard to maintain higher frequencies at large strains. Hence, it is very important to obtain the high strain viscoelastic property of the material.

The high strain modulus can be predicted approximately using strain sweep data. Strain sweep experiments are conducted at a constant frequency at different temperature to obtain the viscoelastic property at different stresses. The viscoelastic property at different strains or stresses at higher frequencies can be obtained by shifting the data at different temperatures using the shift factor calculated at lower temperature. An implicit equation [33] for stress at 100% strain is obtained as a function of the average RMS surface slope $\kappa(q)$ given by,

$$\sigma(\omega) = \sigma_0 + 0.67\,\kappa(q)|E(\omega,\sigma)| \tag{5.6}$$

Where, $\kappa^2(q) = \int_{q_l}^{q} d^2q' q'^2 C(q')$ and $\sigma_0$ is the nominal pressure. The implicit function is then used to obtain the elastic modulus at large strain (100%). For Compound – A on 120-grit surface the elastic modulus at large strain is as shown in Figure 5.5. The viscoelastic property is then extrapolated to higher frequencies.

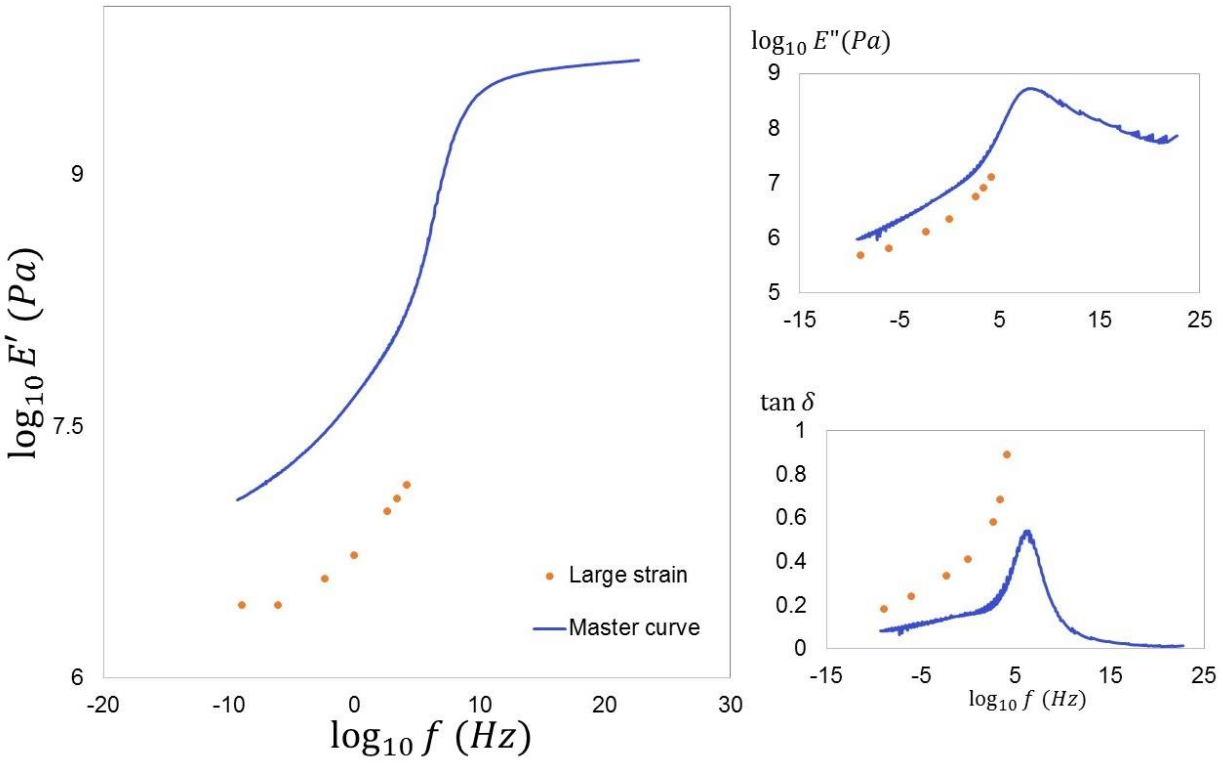


**FIGURE 5.5: LARGE STRAIN MODULUS FROM SMALL STRAIN SHIFT FACTOR AND EQ. (5.6)**

## Surface Roughness Characterization

*Power Spectral Density:*

The power spectral density of the height profile is obtained for 120 grit and asphalt surface as shown in the Figure 5.6 using Eq. (3.15, 3.16). The lower cutoff wave vector is obtained by taking the point below which $C(q)$ tends to be constant. The fractal dimension is then calculated from the slope of PSD curve between the lower and upper cutoff wave vector and then using Eq. (3.18).

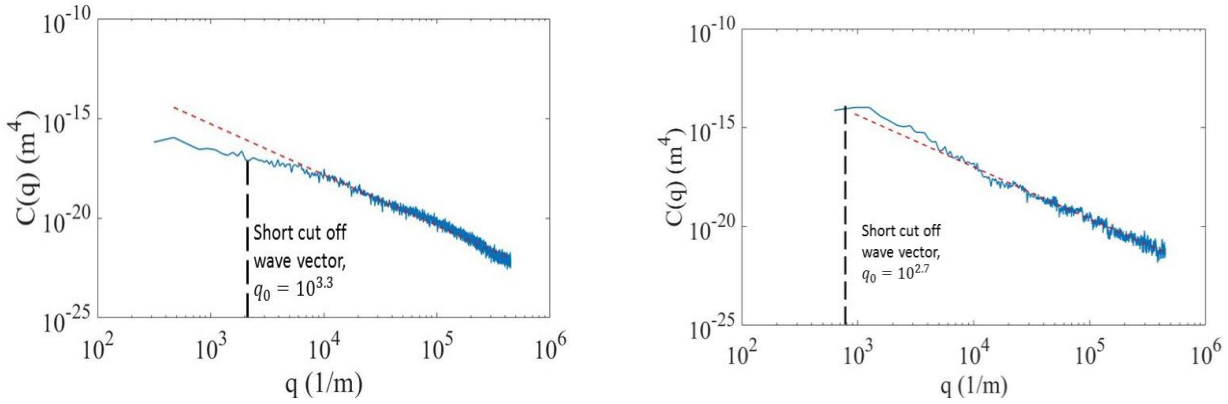


**FIGURE 5.6: POWER SPECTRAL DENSITY OF (A) 120-GRIT (LEFT) AND (B) ASPHALT TRACK (RIGHT)**

The RMS roughness amplitude of the surface is obtained considering the surface to be isotropic and the statistical properties of the surface is translationally invariant using the Eq. (3.17). The surface descriptors for 120 and asphalt surface is given in Table 5.1.

**TABLE 5.1: SURFACE ROUGHNESS PARAMETERS OF THE SURFACE**

| Surface Property | 120 grit | Asphalt |
|---|---|---|
| $h_0\ (m)$ | $7.6573\ e^{-5}$ | $3.3378\ e^{-4}$ |
| $D_{PSD}$ | 2.3 | 2.15 |
| $q_0(1/m)$ | $10^{3.3}$ | $10^{2.7}$ |
| $q_1(1/m)$ | $10^{6}$ | $10^{6}$ |

*Height Difference Correlation Function:*

The height difference correlation function for the 120 grit is obtained from the height profile by considering the steps as low as the resolution at which the height profile is obtained up until the function plateaus using the Eq. (3.12). For a 120-grit surface, the HDCF is as shown in Figure 5.7.

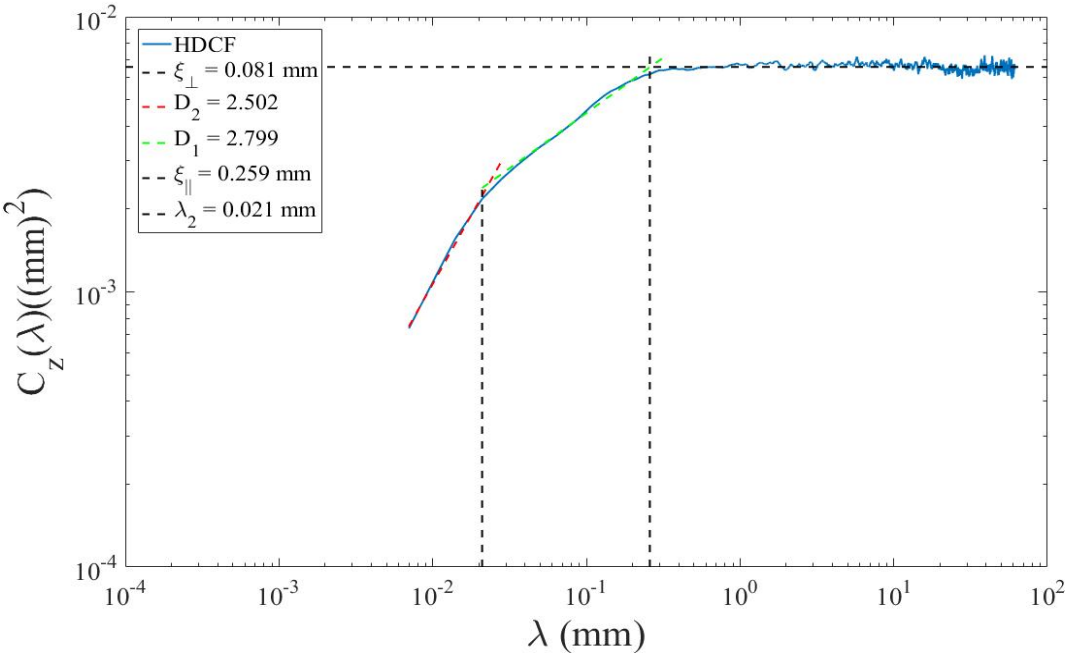


**FIGURE 5.7: HEIGHT DIFFERENCE CORRELATION FUNCTION FOR 120-GRIT SURFACE**

The surface descriptors as obtained from the HDCF for a self-affine surface is given in Table 5.2.

**TABLE 5.2: SURFACE DESCRIPTORS OF 10-GRIT SURFACE FROM HDCF**

| Surface descriptor | Value |
|---|---|
| $\xi_\perp(mm^2)$ | 0.081 |
| $\xi_\parallel(mm)$ | 0.259 |
| $D_1$ | 2.799 |
| $D_2$ | 2.502 |
| $\lambda_2(mm)$ | 0.021 |

### Height Distribution

The height distribution of the 120-grit profile is obtained by considering the experimental data as shown in the Figure 5.8. The affine transformation parameter

is obtained by considering the Eq. (3.20-3.21) in combination with the summit distribution from experimental data. The affine parameter for the 120-grit surface is predicted to be, $s = 1.22$.

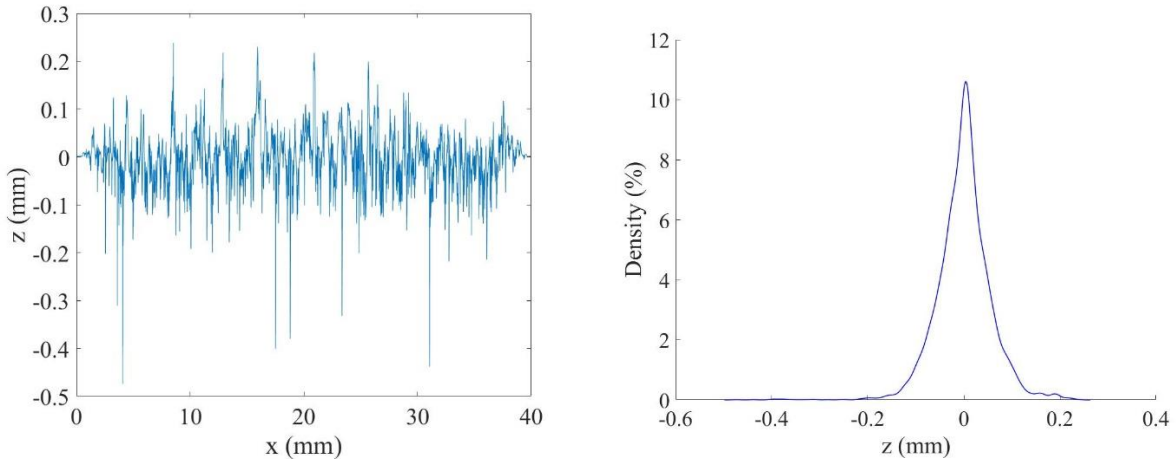


**FIGURE 5.8: (A). HEIGHT PROFILE (LEFT) AND (B). HEIGHT DENSITIES (RIGHT)**

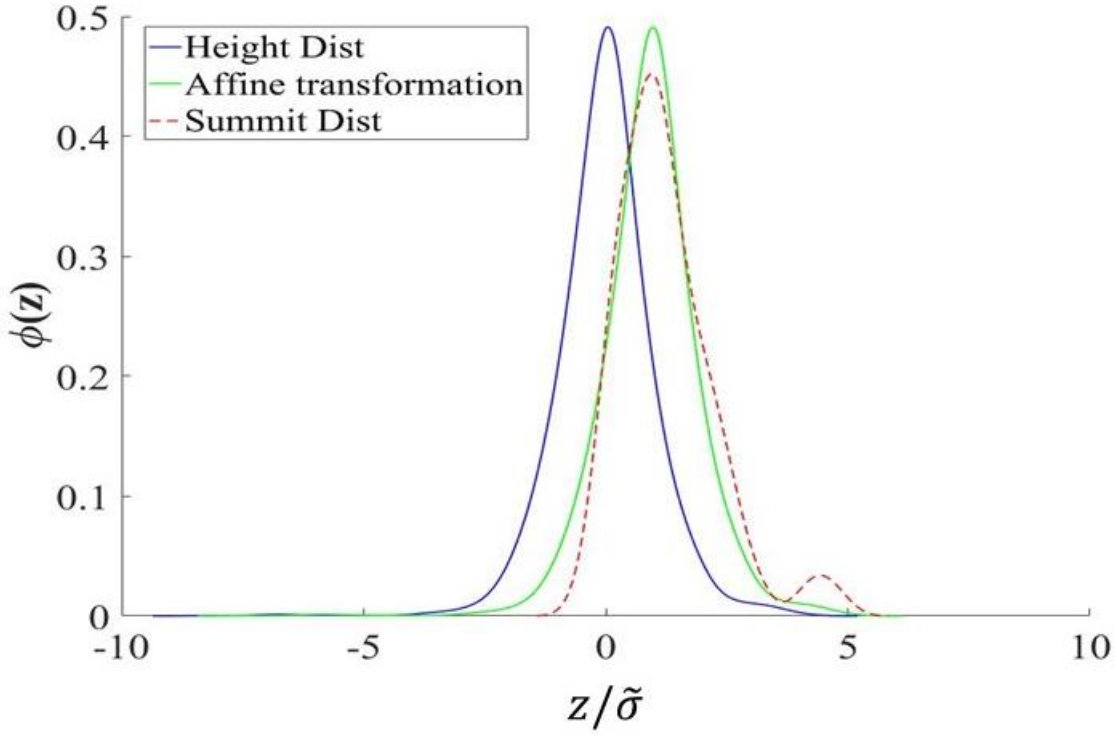


**FIGURE 5.9: AFFINE TRANSFORMATION BASED ON SUMMIT HEIGHT DISTRIBUTION**

In order to obtain the GW function, the data obtained is normalized by the variance of the respective data, the distribution of the normalized data is obtained and this is then used to obtain the GW function given by Eq. (3.10). The result is as shown in the Figure 5.10.

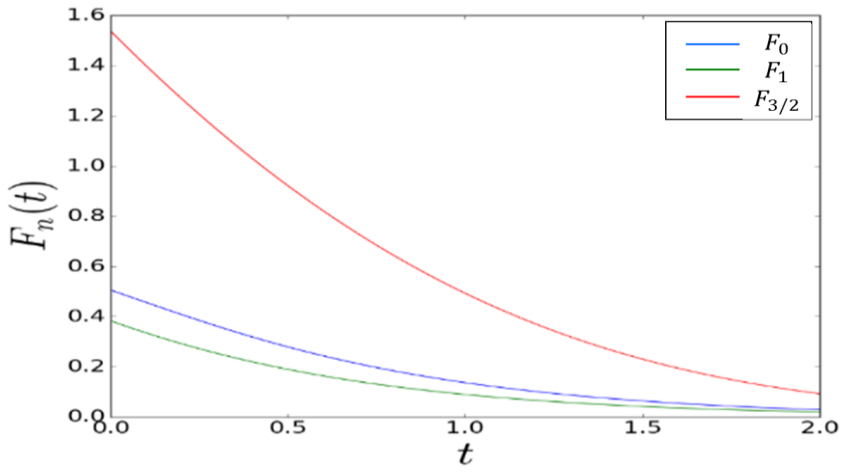


**FIGURE 5.10: GREENWOOD-WILLIAMSON FUNCTION EQ. (3.10)**

## 5.2.SIMULATION RESULTS FOR PERSSON'S FRICTION MODEL

In the previous chapter, the physics behind Persson's Friction Model was discussed. In this section, the simulation results for the friction model is obtained using Python and the variation of the model under different operating conditions are discussed.

### Validation with Persson's Results without flash temperature

The friction model is validated with the results obtained by Persson [29] for a linear viscoelastic model which is represented by the Standard linear solid model where the viscoelastic modulus is given by Eq. (5.7).

$$E(\omega) = \frac{E_1(1 - i\omega\tau)}{1 + a + i\omega\tau} \tag{5.7}$$

Where $E_1 = E(\infty)$, $a$ is the ratio between $E(\infty)/E(0)$ and $\tau$ is the characteristic time. The material and surface parameters used are, $E_1 = 10^9 MPa$, $a = 1000$, $\tau =$

$0.001\,s$, $H = 0.85, q_0 = 1000$ and $q_0 h_0 = 1$. The area ratio is obtained for a nominal pressure $\sigma_0 = 0.04MPa$ as a function of the magnification at five different velocities using the Eq. (3.34),

The Eq. (3.34) is numerical integrated using Simpson rule at different $q$ depending on $\zeta$ using the given parameters. The area ratio as a function of $\zeta$ is as shown in the Figure 5.11 for five different velocities. It compares the simulation results at $\sigma_0 = 0.04MPa$ with Persson's results. The simulated results match very well with Persson's results, as we can see that as the velocity increases the area ratio decreases.

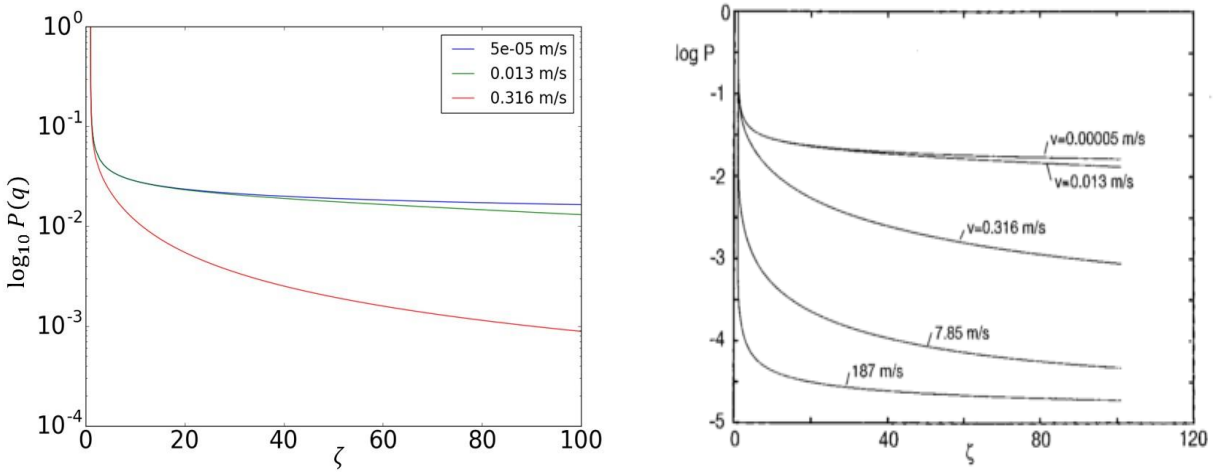


**FIGURE 5.11: AREA RATIO OBTAINED FROM SIMULATION. MODEL RESULTS (LEFT), PERSSON'S RESULTS (RIGHT)**

Similarly, the friction coefficient as a function of velocity at different length scales and Hurst exponent was obtained by solving the Eq. (3.40) using numerical integration for linear viscoelastic material. Figure 5.12 and Figure 5.13 shows the simulated results along with Persson results for the same nominal pressure and the results agree with each other. The friction coefficient increases with an increase in magnification, also the peak friction tries to narrow and decreases with an increase in the Hurst exponent this is because as the Hurst exponent increases the surfaces tend to be smoother and hence the friction reduces.

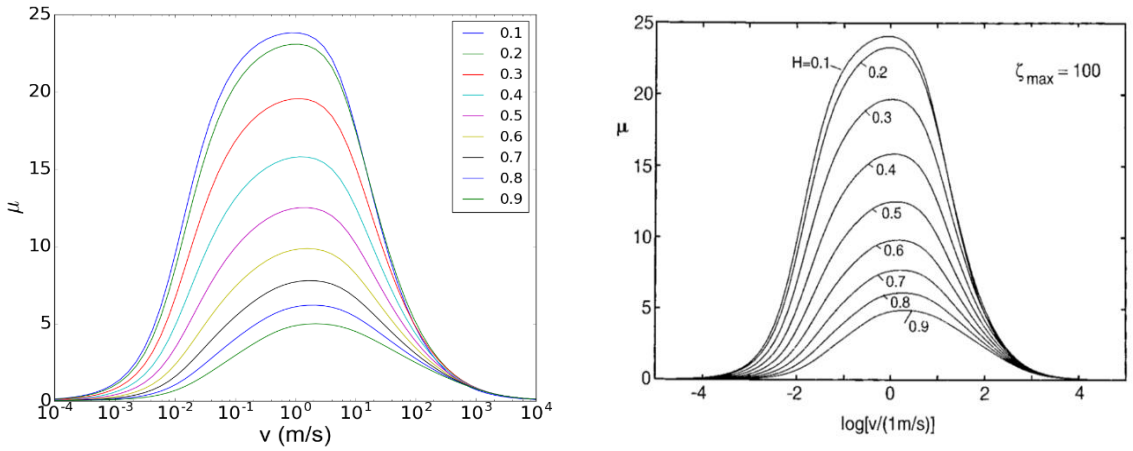


**FIGURE 5.12: FRICTION COEFFICIENT AS A FUNCTION OF HURST EXPONENT. MODEL RESULTS (LEFT), PERSSON'S RESULTS (RIGHT)**

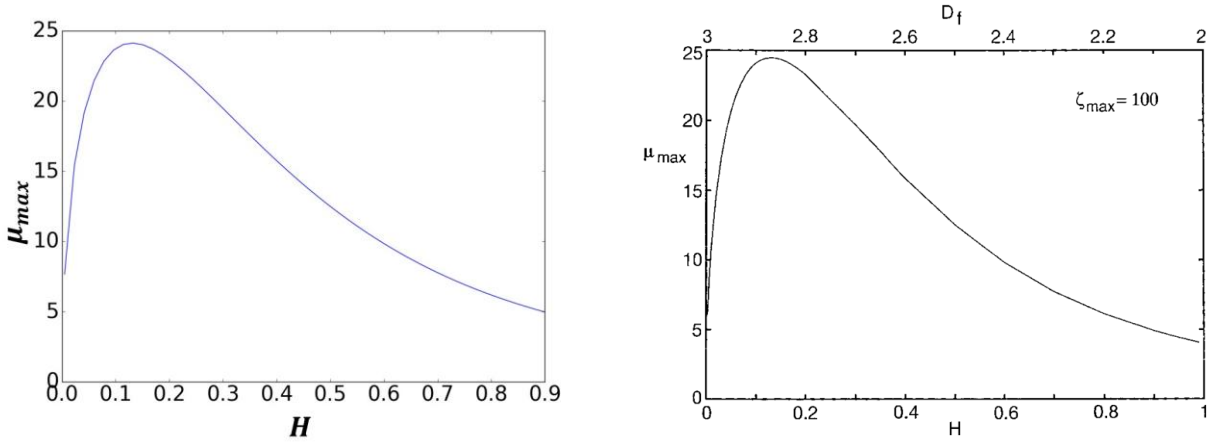


**FIGURE 5.13: MAXIMUM FRICTION VARIATION WITH HURST EXPONENT. MODEL RESULTS (LEFT), PERSSON'S RESULTS (RIGHT)**

## Including Frictional heating

The frictional shear stresses generated in the contact because of the fluctuating forces acting on the rubber due to the undulations in the contact surface will result in energy dissipation at the contact. This energy dissipation results in local heating of rubber, which further leads to temperature rise at the interface. This temperature change at the interface due to localized heating is known as Flash temperature. The

temperature rise due to the local heating will result in a considerable decrease in the viscoelastic modulus of rubber. At very low speeds, the temperature rise is minor due to heat diffusion into the rubber and contact surface, but at high speeds of the order of $10^{-2} m/s$ there is a considerable temperature rise of rubber that will affect the properties and hence cannot be neglected.

The flash temperature or the temperature rise at the contact is predicted as a function of magnification and sliding velocity by solving the implicit equation given by Eq. (3.44) using iterative method. The frictional heating of a filled rubber material on an asphalt surface is considered and validated against the results from Persson [34]. The material parameters for a typical rubber and the surface parameters considered are given in Table 5.3.

**TABLE 5.3: THERMAL PROPERTIES OF A RUBBER COMPOUND AND SURFACE PROPERTIES OF ASPHALT [34]**

| Parameter | Value |
|---|---|
| $\rho\ (kg/m^3)$ | $10^3$ |
| $C_V\ (J\ kg^{-1}K^{-1})$ | $10^3$ |
| $\lambda_k\ (W\ m^{-1}K^{-1})$ | 0.1 |
| $D$ | 2.2 |
| $q_0\ (1/m)$ | 1500 |

The RMS roughness amplitude $h_0$ is obtained from the Eq. (3.17) as used in the previous section. False position method is used to estimate the temperature as a function of magnification and velocity. The lower and upper limit of temperature is to be provided. The lower temperature limit is considered as the background temperature and the upper limit is considered 100-200 C above the background

temperature depending on the sliding velocity. In this case, the background temperature is considered to be $60^oC$ and the upper limit is considered to be $160^oC$ and the simulation is run for sliding velocities between $10^{-6}\ to\ 10^2\ m/s$.WLF shift factor with $C_1 = 8.86$ and $C_2 = 101.6\ K$ is used to obtain the material properties.

The temperature for a sliding velocity is obtained by considering predicted upper and lower limit of the temperature for obtaining the material properties. The temperature estimated is compared with the predicted values. The new predicted temperature is obtained using the false position method given by Eq. (5.8),

$$T_{q,new} = T_u - \frac{f(T_u)(T_u - T_l)}{f(T_u) - f(T_l)}, \qquad f(T_u) = T_{qu} - T_u \tag{5.8}$$

This is repeated until the maximum tolerance for a specific velocity is less than $0.01$. The temperature thus obtained is then used to obtain the friction coefficient and area ratio as a function of magnification and velocity. The RMS roughness amplitude is adjusted to $h_0 = 1/3.4\ q_0$ in order to match the temperature result as a function of magnification to the results of Persson. The obtained results for temperature, friction coefficient and area ratio as a function of magnification at a velocity of $1\ m/s$ is shown in Figure 5.14.

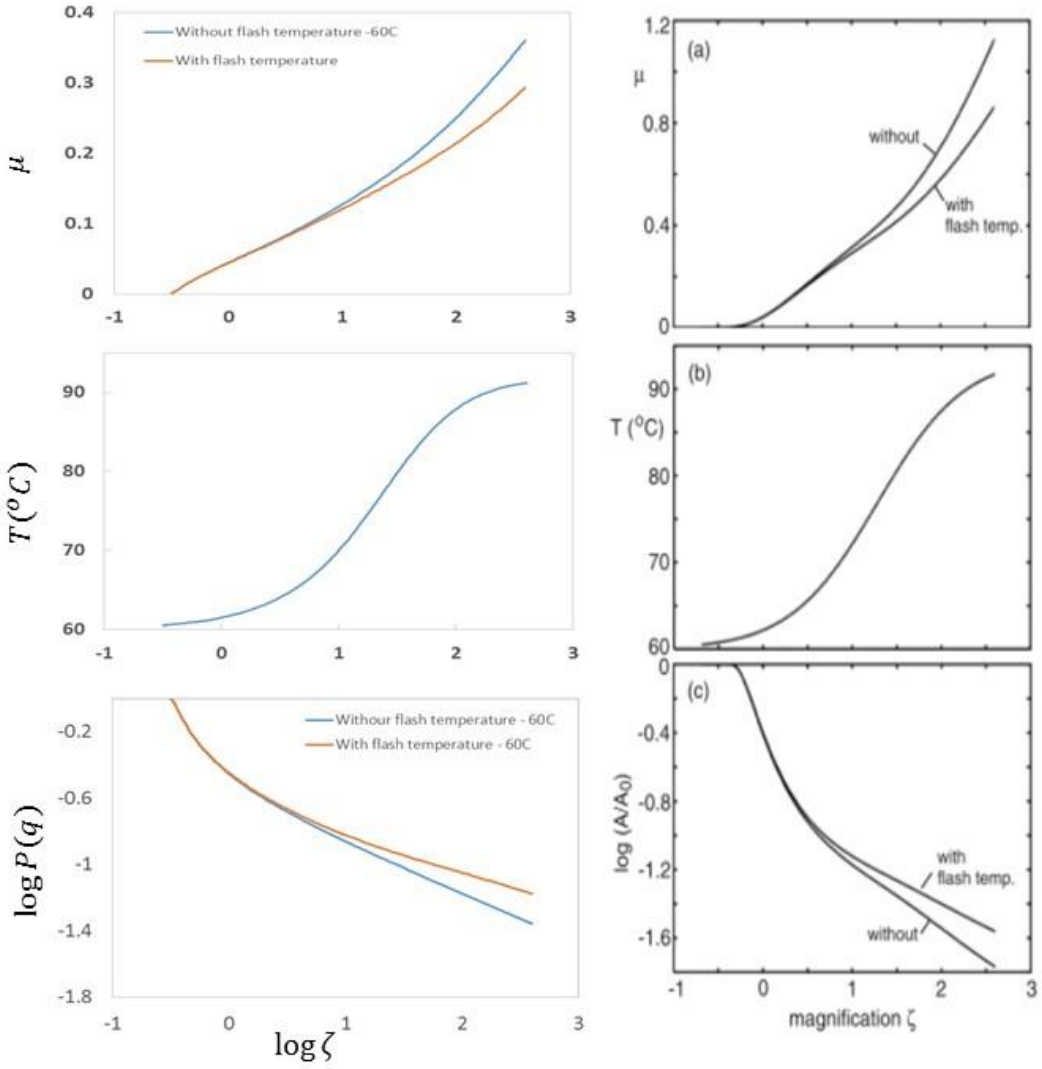


**FIGURE 5.14: VARIATION OF FRICTION, TEMPERATURE AND AREA RATIO WITH MAGNIFICATION. MODEL RESULTS (LEFT), PERSSON'S RESULTS (RIGHT)**

The friction and area ratio results agrees very well with Persson's results qualitatively, but there is a slight difference in the magnitude of the friction and area values. This might be because of the uncertainty of the shift factor of the material that is considered for comparison. The area ratio and temperature as a function of sliding velocity for $\zeta = 1\ and\ 400$ and friction coefficient is simulated and compared with Persson's results as shown in Figure 5.15.

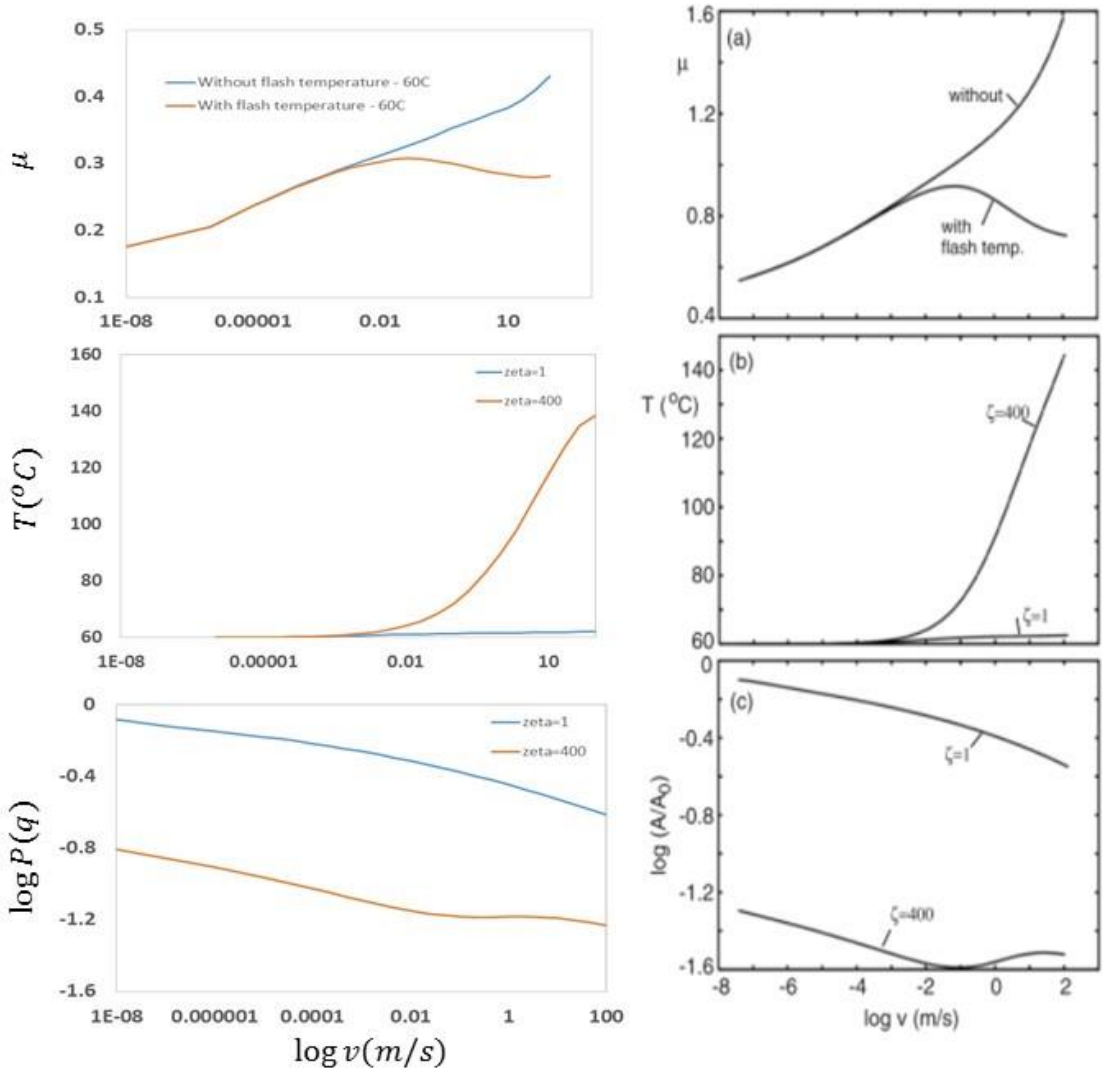


**FIGURE 5.15: VARIATION OF FRICTION, TEMPERATURE AND AREA RATIO WITH VELOCITY. MODEL RESULTS (LEFT), PERSSON'S RESULTS (RIGHT)**

## Compound A on 120 grit surface

In this section, simulation results for a compound A rubber block sliding on a 120-grit surface. The material properties of Compound A was provided by Bridgestone as shown in Figure 5.4. The surface parameters for a 120 grit surface was obtained from the surface profile measured using a Nanovea Profilometer as discussed in sections 4.1, 5.1and given in Table 5.1. Figure 5.16 shows the simulation results for

friction coefficient with and without flash temperature and the temperature rise considering the background temperature $T_0 = 20^oC$ . Figure 5.17 show the temperature as the function of velocity and magnification.

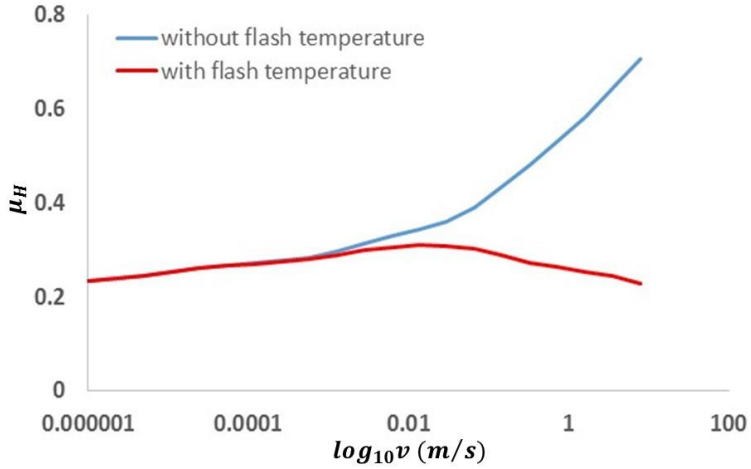


**FIGURE 5.16: FRICTION OF COMPOUND A ON 120-GRIT SURFACE WITH AND WITHOUT FLASH TEMPERATURE**

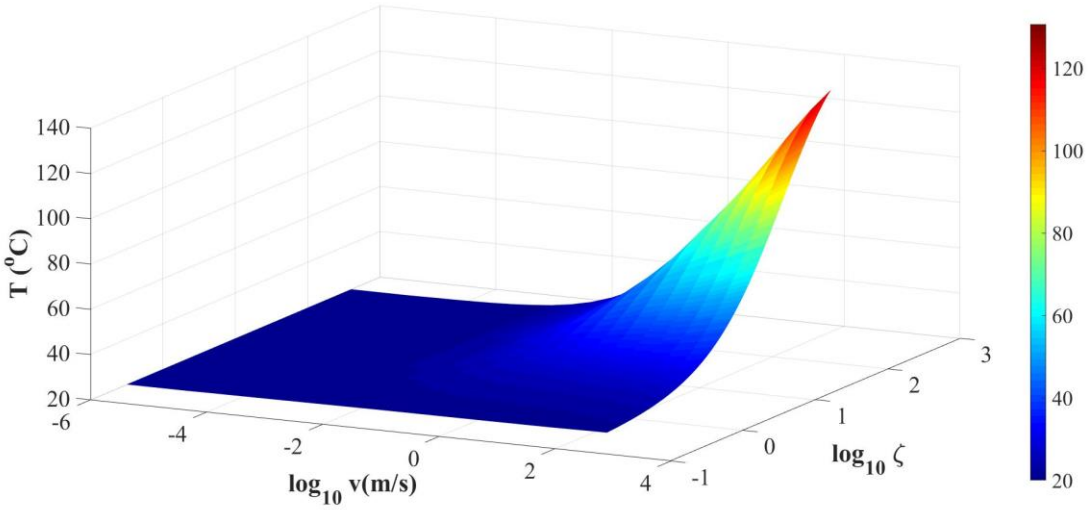


**FIGURE 5.17: TEMPERATURE RISE AS A FUNCTION OF MAGNIFICATION AND VELOCITY**

*Comparison of Small strain - Large strain*

The simulation results by considering large strain elastic modulus is obtained here. Figure 5.18 shows the variation in viscoelastic modulus for small and large strain rates. As seen, the stiffness of the material reduces by an order of magnitude for large strains. The friction coefficient and area ratio is obtained considering small and large strain modulus and the results are shown in Figure 5.19.

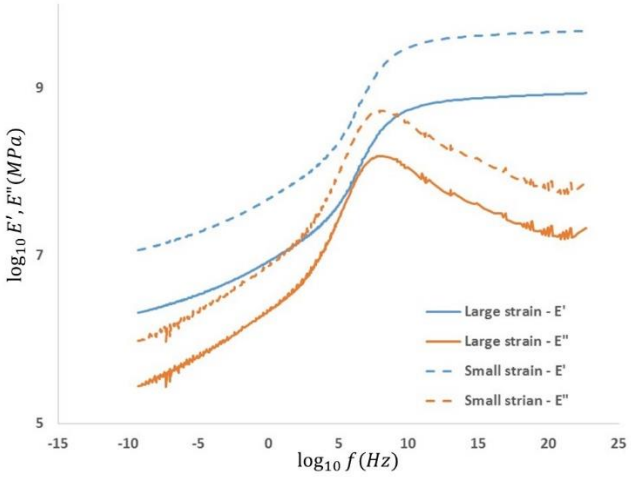


**FIGURE 5.18: SMALL STRAIN VS LARGE STRAIN MODULUS**

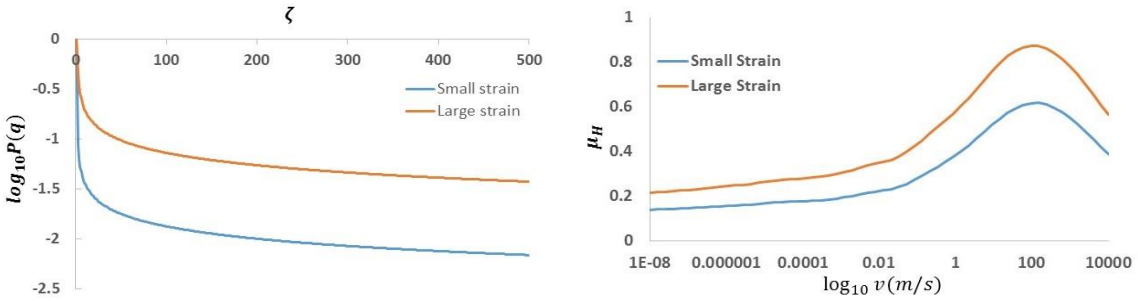


**FIGURE 5.19: (A). AREA RATIO (LEFT) AND (B). FRICTION VARIATION (RIGHT) FOR SMALL AND LARGE STRAIN**

As there is decrease in the stiffness of the material from small to large strain, the material tends to cover more contact area as seen in the area ratio results as shown

in Figure 5.19(A). In addition, the friction coefficient increases for large strain modulus as shown in Figure 5.19(B).

*Variation of Temperature rise with surface parameters:*

While validating Persson's results we have seen the variation of the friction coefficient with Hurst exponent. Here we will see the variation of temperature rise with magnification for different surface parameters. Figure 5.20 shows the variation of the temperature with the RMS roughness amplitude ($h_0$) and Hurst exponent ($H$). As said earlier, as the Hurst exponent increases the surface tends to be smoother and hence the peak temperature decreases which is seen in the results. For $h_0$, as the value increases the roughness of the surface increases and the temperature increases.

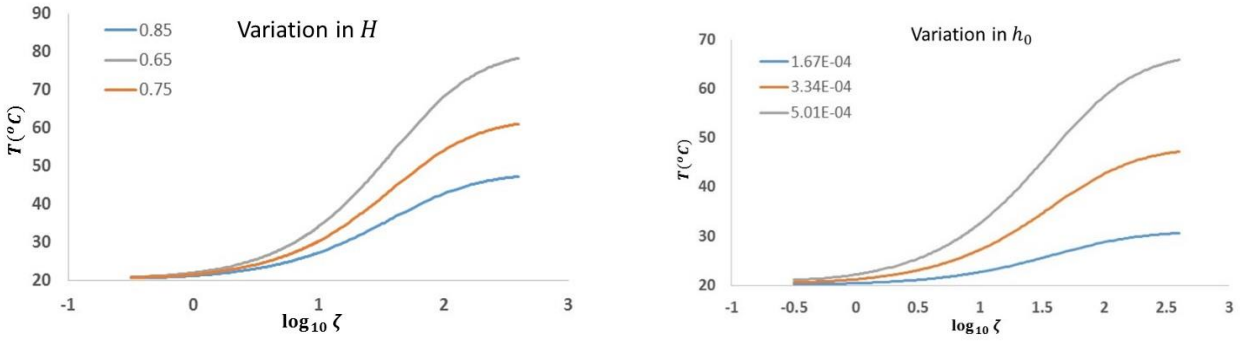


**FIGURE 5.20: TEMPERATURE VARIATION WITH HURST EXPONENT (LEFT) AND RMS ROUGHNESS (RIGHT)**

Figure 5.21 shows the variation of the temperature rise with respect to the low cutoff wave vector. In this case, the maximum magnification is kept constant at $\zeta_{max} = 400$. So hence, with increase in $q_0$ the large cut off wave vector, $q_1$ also increases hence the limit of integrations extends to lower length scales because of which the peak temperature increases.

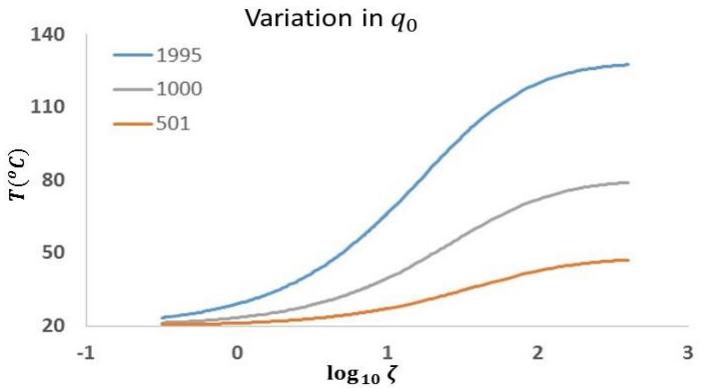


**FIGURE 5.21: TEMPERATURE RISE WITH VARIATION IN LOW CUT-OFF WAVE VECTOR**

*120-grit vs Asphalt Surface:*

Frictional heating is a function of surface roughness. As the roughness in the surface increases, the friction shear stresses on the rubber increases and is the temperature rise. The simulation results of the Compound A on an asphalt surface over a 120-grit surface is shown in Figure 5.22. The surface parameters is given in Table 5.1. The 120 grit is rougher than the asphalt surface and hence the temperature rise and friction coefficient will be higher for 120 grit than the asphalt surface that can be seen from the simulation results.

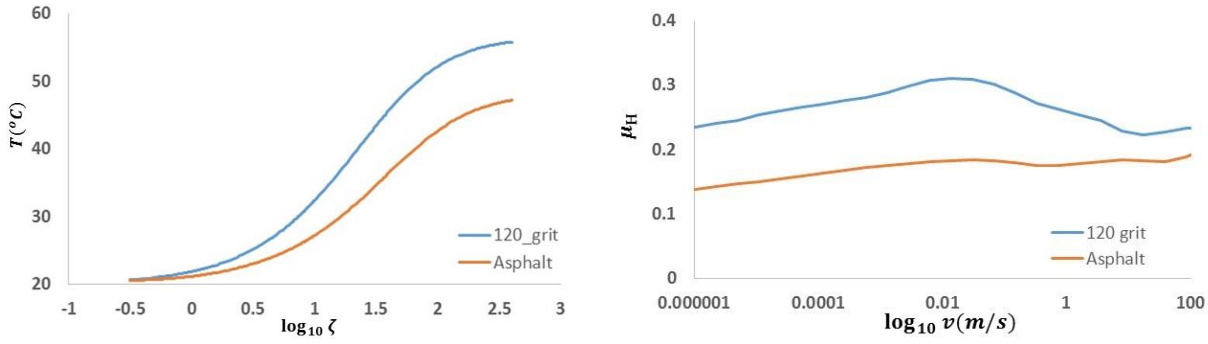


**FIGURE 5.22: TEMPERATURE RISE AND FRICTION FOR TWO DIFFERENT SURFACES**

## 5.3.SIMULATION RESULTS FOR KLUPPEL'S FRICTION MODEL:

The simulation results for the Kluppel's friction model will be obtained for a filled SBR compound on rough granite and Compound A on a 120-grit surface. The former results is for validation of the results with the results from Le Gal [32]. While the latter case will be considered for considering the variation of the model under different conditions of material and surface parameters. The model results will be further compared with the results from Persson's model and experiments.

### Validation with Kluppel' Results

The surface descriptors for a rough granite and material properties for SBR5025 compound with carbon black filled [32] for the strain amplitude of 0.3% for a reference temperature of $T_0 = 23^o C$ is considered. The height distribution for the surface is considered using a normal distribution and the variance is adjusted to match with the experimental distribution from literature as shown in Figure 5.23.

**TABLE 5.4: HDCF OF ROUGH GRANITE FOR 1 AND 2 SCALING REGIMES [32]**

| Parameter | One Scaling regime | Two scaling regime |
|---|---|---|
| $D_1$ | – | 2.37 |
| $D_2$ | 2.14 | 2.14 |
| $\xi_{\parallel}$ | 1.06 | 2.49 |
| $\xi_{\perp}$ | 0.31 | 0.31 |
| $\lambda_2$ | – | 0.093 |
| $s$ | 1.25 | 1.27 |

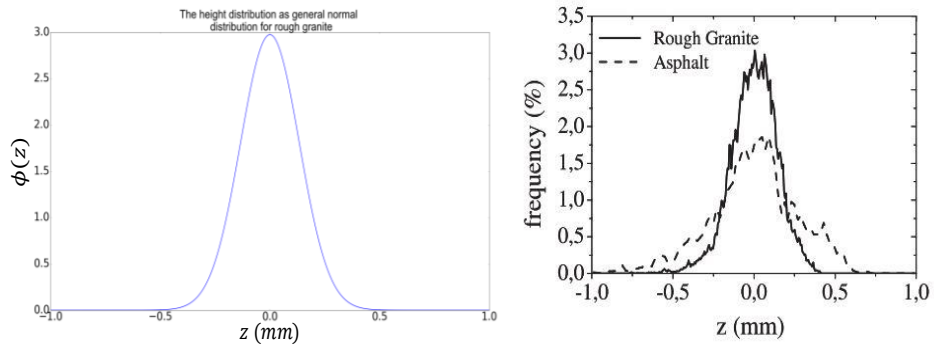


**FIGURE 5.23: GAUSSIAN DISTRIBUTION OF HEIGHT PROFILE FOR ROUGH GRANITE.**

The Greenwood Williamson (GW) function for the height distribution of rough granite is obtained by solving Eq. (3.10). The varying minimum length for a single and two scaling regime as a function of velocity is obtained by using the GW function values and solving the Eq. (3.56). The surface distance is obtained using the hertz contact theory and considering the radius of curvature of the asperity. The minimum wavelength is as shown in Figure 5.24.

The equation is implicit and an iterative method is used to obtain the varying minimum wavelength as a function of velocity. The friction coefficient is obtained from the varying minimum wavelength condition and the mean penetration depth using the Eq. (3.52, 3.54, and 3.56) and the results are shown in Figure 5.25. The grey curve of the right is compared and is seen to match very well with the literature.

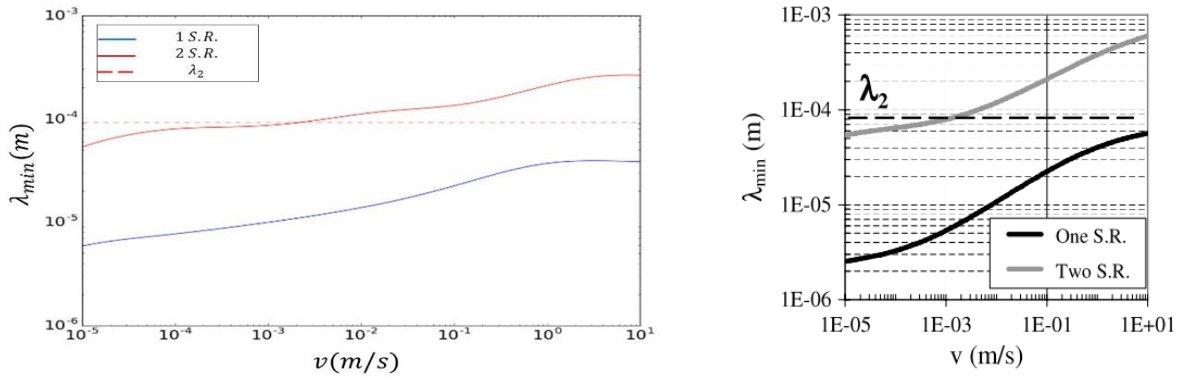


**FIGURE 5.24: VARYING MINIMUM WAVELENGTH AS A FUNCTION OF VELOCITY. MODEL RESULTS (LEFT) LITERATURE RESULT [32] (RIGHT)**

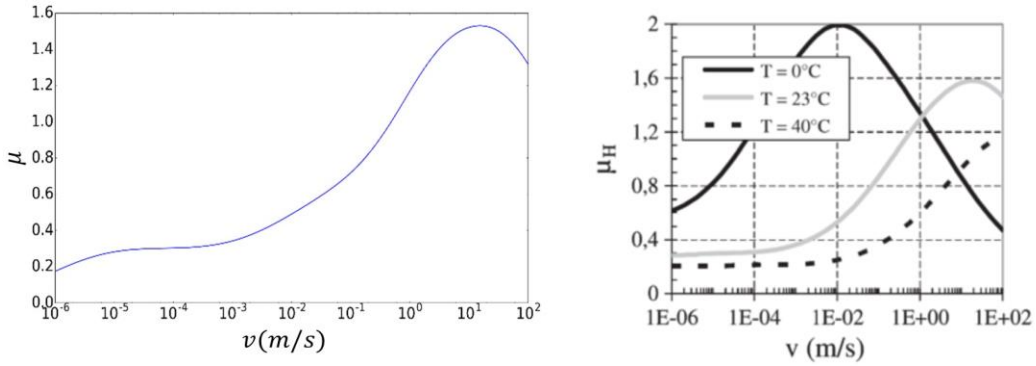


**FIGURE 5.25: FRICTION COEFFICIENT AS A FUNCTION OF VELOCITY. MODEL RESULTS FOR SINGLE REGIME (LEFT) LITERATURE RESULT [32] (RIGHT)**

## Compound A on 120 grit

The simulation results for compound A on a 120 grit surface obtained here. The surface descriptors for the 120-grit surface is obtained using the HDCF and is given in Table 5.2. The height distribution is obtained from the height profile from the Nanovea profilometer. The affine transformation parameters is obtained by using the analytical and numerical method discussed in section (3.2).

The GW function is then obtained by normalizing the height profile data with the variance of the surface height and then getting the experimental distribution from

the normalized values of height. The distribution thus obtained is then used to predict the GW function and is as shown in Figure 5.10.

The GW function is then used to obtain the varying minimum wavelength and the friction coefficient. The material properties for Compound A for the low strain amplitude is used which is as shown in Figure 5.18. The friction coefficient and the varying minimum wavelength for the case of single regime is as shown in Figure 5.26.

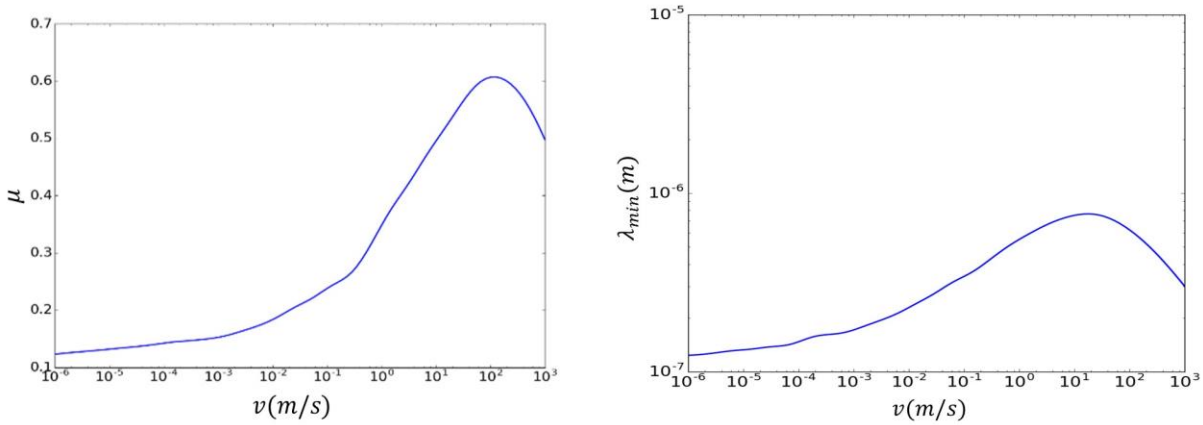


**FIGURE 5.26: KLUPPEL'S FRICTION COEFFICIENT FOR COMPOUND A ON 120-GRIT SURFACE**

The friction coefficient for large and small strain viscoelastic modulus is compared and the variation of length scale range considered for the case of large strain modulus. The friction coefficient is higher for the large strain case as seen in the case of Persson's model and as shown in Figure 5.27. The length scale range has a significant effect on the hysteresis friction depending on the operating condition. As shown in Figure 5.27, the macroscale roughness range is the dominant factor. Consideration of the lower length scale broadens the friction curve mainly at higher loads or lower sliding velocities because of the formation of intimate contact with lower asperities.

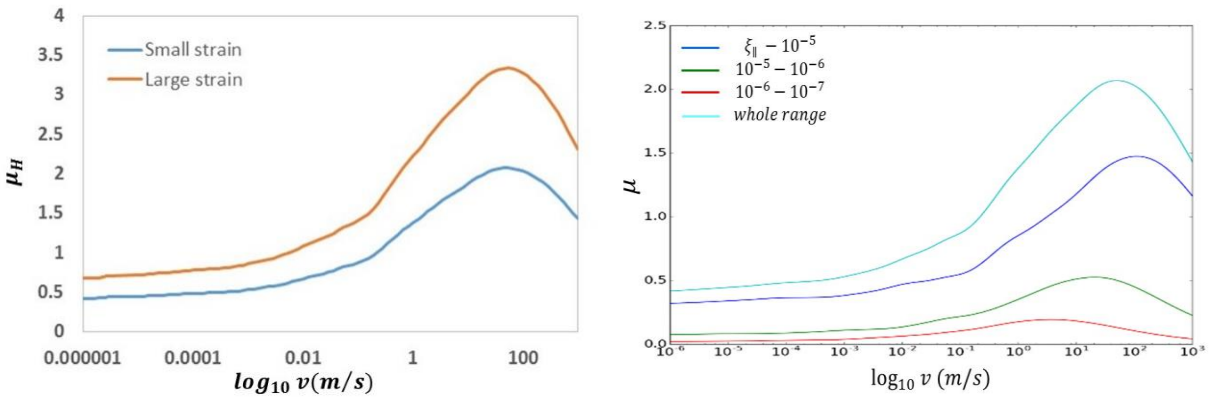


**FIGURE 5.27: VARIATION OF FRICTION WITH LARGE STRAIN VS SMALL STRAIN MODULUS (LEFT) AND LENGTH SCALE RANGE (RIGHT)**

## 5.4. COMPARISON OF PERSSON AND KLUPPEL'S MODE AND VALIDATION WITH EXPERIMENT

The friction coefficient obtained for Persson and Kluppel is compared for the case of Compound A on 120-grit surface. The simulation results along with the experimental results of friction obtained using the Dynamic friction tester as shown in Figure 5.28 without including the flash temperature for the theoretical case. The Kluppel's friction coefficient has an overestimation peak friction than the Persson. This is mainly because of considering the contact to be only at the summits of the asperities and considering the asperities to have identical radius of curvature in Kluppel.

The above simulation results were only considering the hysteresis losses in the material. The adhesion part of the friction has to be considered for comparing with the experimental results. A semi empirical adhesion friction model is considered as given in Eq. (5.9). The empirical constants are obtained using the experimental

friction results and the theoretical hysteresis friction results. The empirical constants for a similar case is taken from literature as given in Table 5.5.

Semi empirical Adhesion friction [21] and including flash temperature to it

$$\mu_{adh} = \frac{\tau_f}{\sigma_0} P(\zeta, v, T)$$
$$\tau_f = \tau_{f0} \exp\left(-c \left[\log_{10}\left(\frac{v}{v_0}\right)\right]^2\right) \quad (5.9)$$

For a 120-grit surface the empirical constants are given by,

**TABLE 5.5: EMPIRICAL CONSTANTS [21]**

| Empirical constant | Value |
|---|---|
| $\tau_{f0}(MPa)$ | 8.3 |
| $c$ | 0.1 |
| $v_0(m/s)$ | $6\ e^{-3}$ |

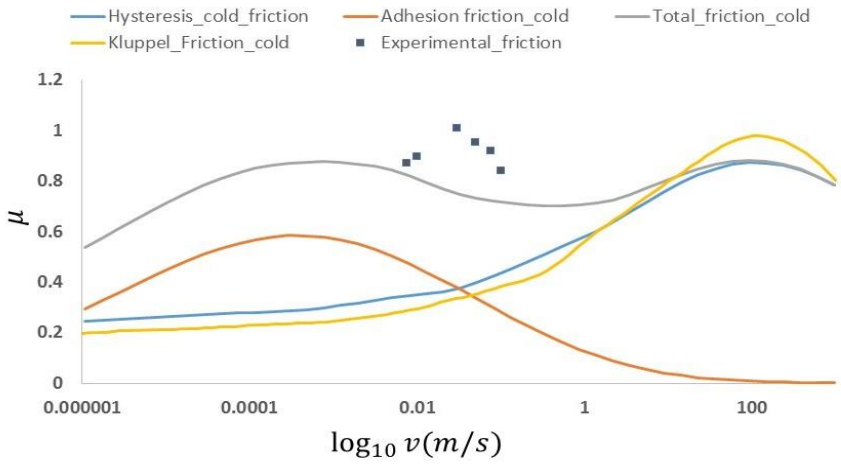


**FIGURE 5.28: COLD FRICTION: PERSSON AND KLUPPEL WITH EXPERIMENTAL**

Including the adhesion friction the total friction without including the flash temperature is obtained and is as shown in the Figure 5.29. The friction coefficient

for the case of including the flash temperature is considered where the peak of the hysteresis friction shifted to lower velocities and the friction values seems to be closer to the experimental values.

The temperature is obtained by assuming there is no heat diffusion from rubber to the road surface. However, in actual case the temperature diffuses in both direction and hence the temperature diffusion into the surface is to be considered. The adhesion constants are also dependent on the variation in the testing conditions and either experiments for the exact conditions is to be considered to obtain the empirical constants or theoretical model for adhesion should be used that considers the interfacial energy to obtain the friction in adhesion.

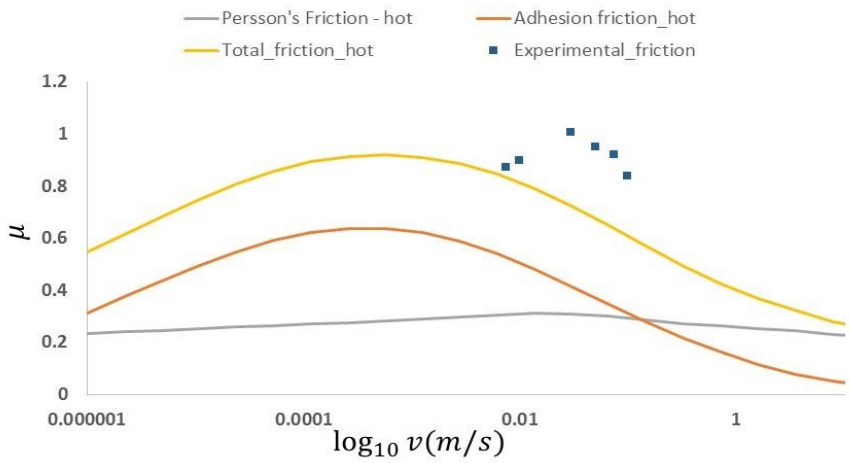


**FIGURE 5.29: HOT FRICTION - PERSSON WITH EXPERIMENTAL**

# 6. CONCLUSION

Contact friction plays a vital role for estimation of tire traction, rolling resistance, tire wear and vehicle dynamics. Frictional behavior of tires is very different from other material due to viscoelastic behavior of rubber resulting in dynamic complex moduli. Experimental investigations in the past have shown the dependence of various factors on tire contact friction like operating condition – normal load, sliding velocity, background temperature, nature of surface and material conditions – complex dynamic moduli, temperature dependence, and material composition. It mainly comprises of hysteresis component and adhesion component, where hysteresis is highly material dependent and adhesion is dependent on the interfacial properties. Empirical formulations based on experimental behaviors though accurate are highly dependent on the conditions at which the empirical constants are estimated.

Rubber friction is governed by energy dissipated due to deformations at the rubber surface and contact mechanics, which is further, governed by complex dynamic moduli of rubber, nature of surface and boundary conditions. Complex dynamic moduli of a viscoelastic material can be represented either by a linear viscoelastic model, where the material is modeled using a linear combination of springs and dampers to represent the elastic and viscous response. It can also be obtained using Dynamic Mechanical Analysis of a rubber sample at different frequency and temperature sweeps and using Time Temperature Superposition for extending it to wide range of frequencies.

Contact mechanics mainly defines the true area of contact and the average stress distribution at the contact interface for the forces acting at the interface. The deformations at the contact is obtained by assuming a point contact on an elastic half space. Elastic contact conditions based on the profile of the surface is then used to

obtain real area of contact, average stress distribution and mean penetration depth. Surface profile initially considered spherical was later expanded for surfaces with randomly rough surfaces. Surface height profile measured using Nanovea profilometer was characterized to obtain the surface parameters assuming the surface as self-affine.

Persson and Kluppel developed friction models in order to predict the hysteresis component of rubber friction. Energy dissipated from the internal oscillations of the rubber due to the undulations of the surface was related the frictional shear stress at the surface. Constitutive relations were developed to obtain the relation between stress and displacement in the frequency domain. Deformation of rubber considered to follow the profile of the substrate and related to the surface characteristics. Persson uses surface roughness power spectrum and Kluppel uses height correlation function to obtain the surface characteristics. The contact parameters are estimated using contact theories. Kluppel uses an extension of Greenwood Williamson theory to include the effects of neighboring asperities. Persson develops a contact theory based on the stress probability distribution at the contact interface. Temperature rise due to the frictional shear stress generated is included based on heat diffusion relation.

Simulated results of the generated model are validated with the results from the literature. Frictional behavior of Compound A – filled synthetic rubber under different conditions of strains, temperature and surfaces is predicted. Including the temperature effect shifts the modulus property of the material that changes the friction coefficient. Simulation results are compared with experimental results obtained from Dynamic friction tester on 120-grit surface with and without frictional heating. The hysteresis friction results were far off from the experimental obtained results because adhesion component of the friction is stronger at low velocities that

is not included in the model. Semi-empirical adhesion model was included using the empirical constants for a similar material in which closer agreement with the experimental results was found but at higher velocities the error increases. This can be due to the assumptions considered in the theoretical model for which stationary sliding, no heat diffusion to the surface, the empirical constants vary with slight variation in the conditions and the model is developed for a sliding rubber block. But, the experiments were conducted for a round rubber sample under rolling condition in which case we have a stick - slip region that may not obey the stationary sliding condition. Persson's model also assumes the deformations of rubber to follow the substrate profile, which is the case of a complete contact, and the friction coefficient does not vary with load as shown in Figure 6.1. However, experimental results as shown in Figure 6.2 obtained using the Dynamic Friction tester and in literature [35-37] has shown a reduction in the friction coefficient as the load increases.

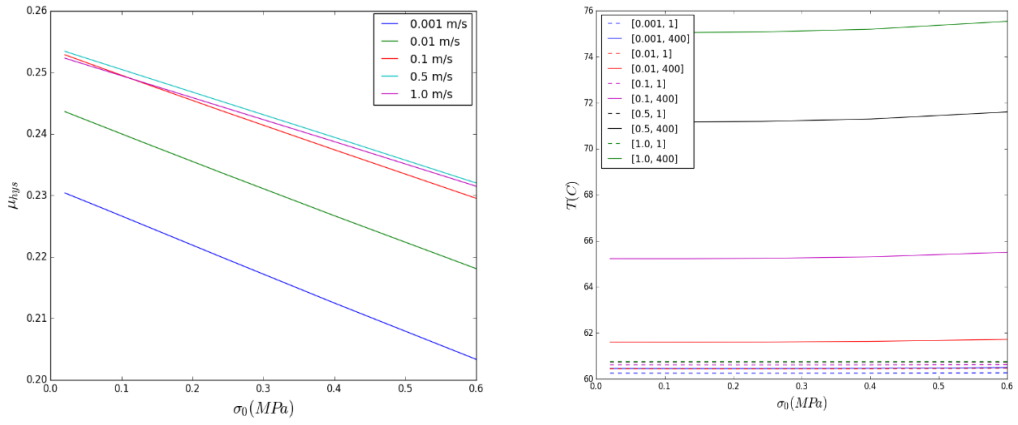


**FIGURE 6.1: SIMULATION RESULTS OF FRICTION COEFFICIENT (LEFT) AND TEMPERATURE RISE (RIGHT) AS A FUNCTION OF NORMAL PRESSURE.**

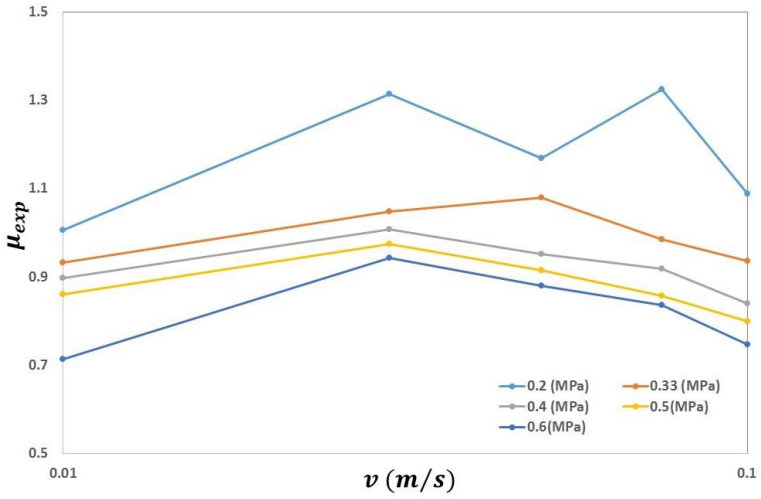


**FIGURE 6.2: EXPERIMENTAL RESULTS FROM DYNAMIC FRICTION TESTER.**

## FUTURE WORKS

Experimental measurements show a variation in the friction coefficient with nominal pressure, but in the case of Persson's friction model the friction coefficient and the temperature does not seem to vary with the variation in pressure especially at lower loads. This is because in the friction model and in the contact mechanics theory develop Persson assumes the deformations to follow the substrate of the surface profile which might be true for lower magnifications but at macro scale the rubber does fill in the cavities of the surface as shown in the Figure 6.3.

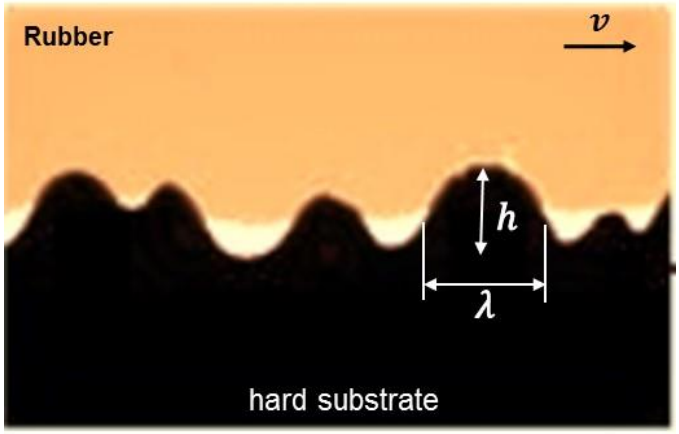


**FIGURE 6.3: PARTIAL CONTACT OF RUBBER WITH CONTACT INTERFACE**

Experimental results are obtained using round samples may not exactly match with the theoretical assumptions considered. Under rolling conditions, we have a stick and a slip region at the contact that might not agree with the assumption of stationary sliding of the model. In addition, for round samples, increase in the normal load changes the nominal contact area, but in the case of rubber block, the nominal contact area is considered to be stabilized and is not effected by change in load.

Linear sliding friction testing under controlled environments has to be considered for the experimental conditions for exact comparison with the theoretical model assumptions. In addition, the load dependency has to be included in the theoretical friction model by considering the deformations of the rubber as a function of the load at macro scale while obtaining the true area of contact using the stress probability distribution.

# REFERENCES


1. Schallamach, A., *The load dependence of rubber friction.* Proceedings of the Physical Society. Section B, 1952. **65**(9): p. 657.
2. Schallamach, A., *The velocity and temperature dependence of rubber friction.* Proceedings of the Physical Society. Section B, 1953. **66**(5): p. 386.
3. Pitenis, A.A., D. Dowson, and W.G. Sawyer, *Leonardo da Vinci's Friction experiments: an old story acknowledged and repeated.* Tribology Letters, 2014. **56**(3): p. 509-515.
4. Grosch, K., *The relation between the friction and viscoelastic properties of rubber*. Rubber Chemistry and Technology, 1964. **37**(2): p. 386-403.
5. Bowden, F.P. and D. Tabor, *The friction and lubrication of solids*. Vol. 1. 2001: Oxford university press.
6. Rabinowicz, E., *Friction and wear of materials.* 1965.
7. Dowling, N.E., *Mechanical Behavior of Material , 2007.* USA.
8. Ferry, J.D., *Viscoelastic properties of polymers*. 1980: John Wiley & Sons.
9. Menard, K.P., *Dynamic mechanical analysis: a practical introduction*. 2008: CRC press.
10. Naya, S., et al., *New method for estimating shift factors in time–temperature superposition models.* Journal of thermal analysis and calorimetry, 2013. **113**(2): p. 453-460.
11. Lorenz, B., W. Pyckhout-Hintzen, and B. Persson, *Master curve of viscoelastic solid: Using causality to determine the optimal shifting procedure, and to test the accuracy of measured data.* Polymer, 2014. **55**(2): p. 565-571.

12. Williams, M.L., R.F. Landel, and J.D. Ferry, *The temperature dependence of relaxation mechanisms in amorphous polymers and other glass-forming liquids.* J. Am. Chem. Soc, 1955. **77**(14): p. 3701-3707.
13. Persson, B.N. and E. Tosatti, *Qualitative theory of rubber friction and wear.* The Journal of Chemical Physics, 2000. **112**(4): p. 2021-2029.
14. Savkoor, A.R., *Dry Adhesive Friction of Elastomers: A study of the fundamental mechanical aspects*. 1987, TU Delft, Delft University of Technology.
15. Grosch, K., *Abrasion of rubber and its relation to tire wear*. Rubber chemistry and technology, 1992. **65**(1): p. 78-106.
16. van der Steen, R.R., *Enhanced friction modeling for steady-state rolling tires.* 2010.
17. Smith, K., R. Kennedy, and S. Knisley, *Prediction of Tire Profile Wear by Steady-State FEM 5.* Tire Science and Technology, 2008. **36**(4): p. 290-303.
18. Hofstetter, K., et al., *Sliding behaviour of simplified tire tread patterns investigated by means of FEM.* Computers & structures, 2006. **84**(17): p. 1151-1163.
19. Cho, J. and B. Jung, *Prediction of Tread Pattern Wear by an Explicit Finite Element Model 3.* Tire science and Technology, 2007. **35**(4): p. 276-299.
20. Motamedi, M., S. Taheri, and C. Sandu, *Rubber–Road Contact: Comparison of Physics-Based Theory and Indoor Experiments.* Tire Science And Technology, 2016. **44**(3): p. 150-173.
21. Lorenz, B., et al., *Rubber friction: comparison of theory with experiment.* The European Physical Journal E, 2011. **34**(12): p. 1-11.
22. Johnson, K.L. and K.L. Johnson, *Contact mechanics*. 1987: Cambridge university press.

23. Greenwood, J. and J. Williamson. *Contact of nominally flat surfaces*. in *Proceedings of the Royal Society of London A: Mathematical, Physical and Engineering Sciences*. 1966. The Royal Society.
24. Kendall, K., *The adhesion and surface energy of elastic solids.* Journal of Physics D: Applied Physics, 1971. **4**(8): p. 1186.
25. Bush, A., R. Gibson, and T. Thomas, *The elastic contact of a rough surface.* Wear, 1975. **35**(1): p. 87-111.
26. Heinrich, G., *Hysteresis friction of sliding rubbers on rough and fractal surfaces.* Rubber chemistry and technology, 1997. **70**(1): p. 1-14.
27. Klüppel, M. and G. Heinrich, *Rubber friction on self-affine road tracks.* Rubber chemistry and technology, 2000. **73**(4): p. 578-606.
28. Persson, B.N., *On the theory of rubber friction.* Surface Science, 1998. **401**(3): p. 445-454.
29. Persson, B.N., *Theory of rubber friction and contact mechanics.* The Journal of Chemical Physics, 2001. **115**(8): p. 3840-3861.
30. Persson, B. and R. Ryberg, *Brownian motion and vibrational phase relaxation at surfaces: CO on Ni (111).* Physical Review B, 1985. **32**(6): p. 3586.
31. Yang, C. and B. Persson, *Contact mechanics: contact area and interfacial separation from small contact to full contact.* Journal of Physics: Condensed Matter, 2008. **20**(21): p. 215214.
32. Le Gal, A. and M. Klüppel, *Investigation and modelling of rubber stationary friction on rough surfaces.* Journal of Physics: Condensed Matter, 2007. **20**(1): p. 015007.
33. Lorenz, B., et al., *Rubber friction for tire tread compound on road surfaces.* Journal of Physics: Condensed Matter, 2013. **25**(9): p. 095007.
34. Persson, B.N., *Rubber friction: role of the flash temperature.* Journal of Physics: Condensed Matter, 2006. **18**(32): p. 7789.

35. Fortunato, G., et al., *On the dependency of rubber friction on the normal force or load: theory and experiment.* arXiv preprint arXiv:1512.01359, 2015.
36. Fortunato, G., et al., *General theory of frictional heating with application to rubber friction.* Journal of Physics: Condensed Matter, 2015. **27**(17): p. 175008.
37. Braun, O., et al., *On the dependency of friction on load: Theory and experiment.* EPL (Europhysics Letters), 2016. **113**(5): p. 56002.

# APPENDIX

## A. APPENDIX – STRESS – DISPLACEMENT RELATIONSHIP

The derivation of the stress-strain relationship obtained for a linear isotropic elastic medium is obtained by solving the continuity, conservation of momentum and energy equation for the prescribed boundary condition of the surface stress distribution $\sigma_i = \sigma_{3i}$ at $z = 0$. The momentum equation is given by Eq. (A.1),

$$\rho \frac{\partial^2 u}{\partial t^2} = \hat{\mu}\nabla^2 \boldsymbol{u} + \left(\hat{\mu} + \hat{\lambda}\right)\nabla\nabla.\boldsymbol{u}$$
$$\hat{\mu}\phi(t) = \int_{-\infty}^{\infty} dt' \mu(t - t')\phi(t') \tag{A.1}$$

In order to solve the above equation, Fourier transformation of the equations from time to frequency domain is performed.

$$-\rho\omega^2 \boldsymbol{u} = \mu(\omega)\boldsymbol{\nabla}^2 \boldsymbol{u} + (\mu(\omega) + \lambda(\omega))\boldsymbol{\nabla\nabla}.\boldsymbol{u} \tag{A.2}$$
$$u(x, \omega) = \frac{1}{2\pi} \int dt\, u(x, t) e^{i\omega t}$$

Where the lame's constant $\lambda$ and $\mu$ are the frequency dependent material properties given by,

$$\mu = \frac{E(\omega)}{2(1 + \nu)}; \quad \lambda = \frac{\nu E(\omega)}{(1 + \nu)(1 - 2\nu)}$$

The variation of the Poisson's ratio with frequency is small and is neglected. Considering propagation of 3D plane waves the Eq. (A.1) can be represented by the transverse$(c_T)$ and longitudnal$(c_L)$ wave speeds by considering,

$$c_T^2 = \frac{\mu}{\rho}; \quad c_L^2 = \frac{\mu + 2\lambda}{\rho}$$

In order to solve the momentum equation given by Eq. (A.1), it is decoupled by decomposing the displacement field [30] using the form given by Eq. (A.3),

$$\boldsymbol{u} = \boldsymbol{p}A + \boldsymbol{K}B + \boldsymbol{p} \times \boldsymbol{K}\, C \tag{A.3}$$

Where $A, B \; and \; C$ are scalar fields, $\boldsymbol{p} = -i\boldsymbol{\nabla}$, $\boldsymbol{K} = \boldsymbol{n} \times \boldsymbol{p}$ and $\boldsymbol{n}$ is the unit vector normal to the surface. Considering Einstein's notation

$$p_s = -i\frac{\partial}{\partial x_s}; \quad K_s = \varepsilon_{spq} n_p p_q, i.e.,$$

$$\boldsymbol{K} = (p_y, -p_x, 0)$$

$$(\boldsymbol{p} \times \boldsymbol{K})_s = \varepsilon_{spq} p_p \varepsilon_{qmn} n_m p_n = n_s(\boldsymbol{p}.\boldsymbol{p}) - p_s(\boldsymbol{n}.\boldsymbol{p})$$

Hence,

$$u_s = -i\,(A_{,s} + \varepsilon_{spq} n_p B_{,q}) + \left(n_s C_{,jj} - n_j C_{,sj}\right)$$

Substituting in Eq. (A.1) gives,

$$\begin{aligned} -\omega^2\left[-i\left(A_{,s} + \varepsilon_{spq} n_p B_{,q}\right) + \left(n_s C_{,jj} - n_j C_{,sj}\right)\right] \\ = c_T^2 \nabla^2\left[-i\left(A_{,s} + \varepsilon_{spq} n_p B_{,q}\right) + \left(n_s C_{,jj} - n_j C_{,sj}\right)\right] \\ + (c_L^2 - c_T^2)\left[-i\,(A_{,jsj} + \varepsilon_{spq} n_p B_{,qsj})\right] \end{aligned}$$

$$\begin{aligned} -i\left[(\omega^2 + c_L^2\nabla^2)A_{,s} + (\omega^2 + c_T^2\nabla^2)\varepsilon_{spq} n_p B_{,q}\right] \\ + \left[(\omega^2 + c_T^2\nabla^2)\left(-n_s\left(C_{,jj}\right) + n_j C_{,sj}\right)\right] = 0 \end{aligned}$$

The above equation can be written in a matrix form and hence results in,

$$[(\omega^2 + c_L^2\nabla^2)]A = 0$$

$$[(\omega^2 + c_T^2\nabla^2)B] = 0$$

$$[(\omega^2 + c_T^2\nabla^2)C] = 0$$

From the above equations, A is associated with the longitudinal displacement field and B and C are associated with transverse displacement field. Also from Eq. (A.3), $\boldsymbol{K}B$-field is parallel to the $xy$-plane. Taking the fourier transform of the above equation in the spatial domain we get,

$$\begin{aligned} A(\boldsymbol{x}, z, t) &= \int d^2q d\omega\, A(\boldsymbol{q}, \omega)\, e^{i(\boldsymbol{q}.\boldsymbol{x} + p_L z - \omega t)} \\ B(\boldsymbol{x}, z, t) &= \int d^2q d\omega\, B(\boldsymbol{q}, \omega)\, e^{i(\boldsymbol{q}.\boldsymbol{x} + p_T z - \omega t)} \\ C(\boldsymbol{x}, z, t) &= \int d^2q d\omega\, C(\boldsymbol{q}, \omega)\, e^{i(\boldsymbol{q}.\boldsymbol{x} + p_T z - \omega t)} \end{aligned} \tag{A.4}$$

Where,

$$p_T = \pm\left(\frac{\omega^2}{c_T^2} - q^2\right)^{1/2} ; \quad p_L = \pm\left(\frac{\omega^2}{c_L^2} - q^2\right)^{1/2}$$

Considering the constitutive relation for a linear isotropic medium given by Eq. (A.5),

$$\boldsymbol{\sigma} = \lambda\, tr(\boldsymbol{e})\boldsymbol{I} + 2\mu\boldsymbol{e} \tag{A.5}$$

Where $e_{ij} = \frac{1}{2}(u_{i,j} + u_{j,i})$. Taking the surface stress distribution and fourier transforming the equation gives,

$$\sigma_{i3}(x, \omega) = \mu(\omega)(\boldsymbol{n}.\nabla u_i + \nabla_i \boldsymbol{n}.\boldsymbol{u}) + \lambda n_i \nabla.\boldsymbol{u}) \tag{A.6}$$

Multiplying by the $-i$ on both sides;

$$-\boldsymbol{i}\,\boldsymbol{\sigma}(x, \omega) = \mu(\omega)(\boldsymbol{n}.\mathbf{pu} + \boldsymbol{p}(\boldsymbol{n}.\boldsymbol{u})) + \lambda\boldsymbol{n}(\boldsymbol{p}.\boldsymbol{u})) \tag{A.7}$$

Substituting the displacement field in the above stress equation and also considering $\boldsymbol{n} = e_3$, we get;

$$\begin{gathered} \boldsymbol{n}.\boldsymbol{p} = p_z \\ \boldsymbol{n}.\boldsymbol{u} = p_z A + (p^2 - p_z^2)C = p_z A + K^2 C \\ \boldsymbol{p}.\boldsymbol{u} = p^2 A \end{gathered} \tag{A.8}$$

$$-\left(\frac{\boldsymbol{i}}{\boldsymbol{\mu}}\right)\boldsymbol{\sigma} = \boldsymbol{p}(2p_z A + K^2 C) + \boldsymbol{K}\, p_z B + (\boldsymbol{p} \times \boldsymbol{K}) p_z C + \boldsymbol{n}\frac{\lambda}{\mu}\,(p^2 A) \tag{A.9}$$

Obtaining the dot product of Eq. (A.9) with $\boldsymbol{n}, \boldsymbol{K}$, and $\boldsymbol{p}_{\parallel} = (p_x, p_y, 0)$ respectively, we obtain three equation which can be solved to determine the scalar fields A, B and C.

$$\begin{gathered} B = -\frac{i}{\mu}\frac{1}{q^2 p_T}\,\boldsymbol{K}.\boldsymbol{\sigma} \\ A = -\frac{i}{\mu S}\left[2p_T \boldsymbol{q} + \left(\frac{\omega^2}{c_T^2} - 2q^2\right)\boldsymbol{n}\right].\boldsymbol{\sigma} \\ C = -\frac{i}{\mu S}\left[2p_L \boldsymbol{n} - \left(\frac{\omega^2}{c_T^2} - 2q^2\right)\frac{1}{q^2}\boldsymbol{q}\right].\boldsymbol{\sigma} \end{gathered} \tag{A.10}$$

Where,

$$S = \left(\frac{\omega^2}{c_T^2} - 2q^2\right)^2 + 4q^2 p_T p_L$$

Substituting the scalar fields, Eq. (A.10) obtained in the displacement field Eq. (A.3), we finally end up with,

$$\boldsymbol{u}(\boldsymbol{q}, \boldsymbol{\omega}) = M(\boldsymbol{q}, \boldsymbol{\omega})\boldsymbol{\sigma}(\boldsymbol{q}, \boldsymbol{\omega}) \tag{A.11}$$

Where,

$$M = -\frac{i}{\rho c_T^2}\left(\frac{1}{S(q,\omega)}\left[Q(k,\omega)\,(\hat{z}\boldsymbol{q} - \boldsymbol{q}\hat{z}) + \left(\frac{\omega^2}{c_T^2}\right)^2 (p_L \hat{z}\hat{z} + p_T \hat{q}\hat{q})\right] + \frac{1}{p_T}\boldsymbol{e}\boldsymbol{e}\right),$$

Where, $\hat{q} = \frac{\boldsymbol{q}}{q}, \boldsymbol{e} = \hat{z} \times \hat{q}$

$$Q = 2q^2 - \frac{\omega^2}{c_T^2} + 2p_T\, p_L$$

## B. APPENDIX – AREA RATIO

Here we will discuss regarding the derivation of the area ratio. As we discussed the area ratio is related to the stress probability distribution. The stress probability distribution can be written as,

$$p(\sigma, \zeta) = \langle \delta(\sigma - \sigma_1(x)) \rangle \tag{B.1}$$

Increasing the length scale by a small step value will lead,

$$p(\sigma, \zeta + \Delta\zeta) = \langle \delta(\sigma - \sigma_1 - \Delta\sigma) \rangle \tag{B.2}$$

Using the properties of the delta function,

$$p(\sigma, \zeta + \Delta\zeta) = \int d\sigma' \, \langle \delta(\sigma' - \Delta\sigma) \rangle \, \langle \delta(\sigma - \sigma_1 - \sigma') \rangle \tag{B.3}$$

Here the increase in the length scale will increase the stress in the contact proportionally,

$$\langle \Delta\sigma^2 \rangle \propto \Delta\zeta$$

$$\langle \delta(\sigma - \sigma_1 - \sigma') \rangle = p(\sigma - \sigma', \zeta)$$

Fourier transform of $\langle \delta(\sigma' - \Delta\sigma) \rangle = \frac{1}{2\pi} \int dw \, \langle e^{iw(\sigma' - \Delta\sigma)} \rangle$

Using Taylor series expansion on the exponential,

$$\langle e^{iw(\sigma\prime-\Delta\sigma)}\rangle = e^{iw\sigma'}\left(1-\frac{w^2\langle\Delta\sigma^2\rangle}{2}\right)$$

Hence, $\langle\delta(\sigma'-\Delta\sigma)\rangle = \langle\delta(\sigma')\rangle + \frac{1}{2}\frac{\partial^2}{\partial\sigma'^2}\,\langle\delta(\sigma')\rangle\langle\Delta\sigma^2\rangle$

$$p(\sigma,\zeta+\Delta\zeta) = p(\sigma,\zeta) + \frac{\partial p(\sigma,\zeta)}{\partial\zeta} \tag{B.4}$$

Hence

$$p(\sigma,\zeta) + \frac{\partial p(\sigma,\zeta)}{\partial\zeta} = \int d\sigma' p(\sigma-\sigma',\zeta)\left[\langle\delta(\sigma')\rangle + \frac{1}{2}\frac{\partial^2}{\partial\sigma'^2}\,\langle\delta(\sigma')\rangle\langle\Delta\sigma^2\rangle\right]$$

$$p(\sigma,\zeta) + \frac{\partial p(\sigma,\zeta)}{\partial\zeta}\Delta\zeta = \frac{\langle\Delta\sigma^2\rangle}{2}\frac{\partial^2}{\partial\sigma^2}\,p(\sigma,\zeta) + p(\sigma,\zeta)$$

$$\frac{\partial p}{\partial\zeta} = \frac{\langle\Delta\sigma^2\rangle}{2\,\Delta\zeta}\frac{\partial^2 p}{\partial\sigma^2}$$

$$\boldsymbol{\frac{\partial p}{\partial\zeta} = f(\zeta)\frac{\partial^2 p}{\partial\sigma^2}} \tag{B.5}$$

Solving the diffusion relation, Eq. (B.5) to determine the stress probability distribution using the boundary condition,

$$\begin{aligned} p(\sigma,1) &= p_0(\sigma) = \delta(\sigma-\sigma_0) \\ p(0,\zeta) &= 0 = p\big(\sigma_y,\zeta\big) = 0 \end{aligned} \tag{B.6}$$

Multiplying Eq. (B.5) by $\sigma$ and integrating over $\sigma$,

$$\frac{\partial}{\partial\zeta}\int d\sigma\,\sigma\,p(\sigma,\zeta) = f(\zeta)\int_0^\infty \sigma\frac{\partial^2 p}{\partial\sigma^2}d\sigma$$

$$\int_0^\infty \sigma\frac{\partial^2 p}{\partial\sigma^2}d\sigma = \sigma\left[\frac{\partial p}{\partial\sigma}\right]_{\sigma\to0}^{\sigma\to\infty} - \int_0^\infty d\sigma\frac{\partial p}{\partial\sigma}$$

$$= \sigma \left[\frac{\partial p}{\partial \sigma}\right]_{\sigma \to 0}^{\sigma \to \infty} - [p(\sigma \to \infty, \zeta) - p(0, \zeta)]$$

$$\frac{\partial}{\partial \zeta} \int d\sigma \, \sigma \, p(\sigma, \zeta) = 0$$

$$\int d\sigma \, \sigma \, p(\sigma, \zeta) = const \tag{B.7}$$

Substituting the initial condition, $p(\sigma, 1) = p_0(\sigma) = \delta(\sigma - \sigma_0)$

$$\int d\sigma \, \sigma \, p(\sigma, 1) = \int d\sigma \, \sigma \, \delta(\sigma - \sigma_0) = \sigma_0 \tag{B.8}$$

Hence,

$$\int \boldsymbol{d\sigma \, \sigma \, p(\sigma, \zeta) = \sigma_0} \tag{B.9}$$

Now,

$$f(\zeta) = \frac{\langle \Delta\sigma^2 \rangle}{2 \, \Delta\zeta}$$

$$\langle \Delta\sigma_z^2 \rangle = \int d^2q [M_{zz}(q, \omega)]^{-1} [M_{zz}(q, \omega)]^{-1} u(q, \omega) u(q, \omega)$$

Now considering that the rubber fills the asperities completely, $u = h(x)$

$$\langle \Delta\sigma_z^2 \rangle = \int d^2q [M_{zz}(q, \omega)]^{-1} [M_{zz}(q, \omega)]^{-1} \langle h(q) h(q) \rangle$$

$$\langle \Delta\sigma_z^2 \rangle = \frac{1}{4} \int dq q^3 C(q) \int d\phi \left| \frac{E(qv\cos\phi)}{1 - \nu^2} \right|^2$$

$$f(\zeta) = \frac{\langle \Delta\sigma^2 \rangle}{2 \, \Delta q} q_L = \frac{1}{8} q_L q^3 C(q) \int d\phi \left| \frac{E(qv\cos\phi)}{1 - \nu^2} \right|^2 \tag{B.10}$$

Now assuming a solution for the stress probability distribution and then solving Eq. (B.5) it using the boundary condition,

$$p = \sum_{\{n=1\}}^{\infty} A_n(\zeta) \sin\left(\frac{n\pi\sigma}{\sigma_y}\right) \tag{B.11}$$

Substituting in the diffusion relation and then integrating it over $\zeta$,

$$A_n(\zeta) = A_n(1) \exp\left[-\left(\frac{n\pi}{\sigma_y}\right)^2 \int_1^{\zeta} d\zeta' f(\zeta')\right] \tag{B.12}$$

Substituting in Eq. (B.11) and then considering the initial condition,

$$A_n(1) = \frac{2}{\sigma_y} \int_0^{\sigma} d\sigma\, p_x(\sigma) \sin\left(\frac{n\pi\sigma}{\sigma_y}\right) = \frac{2}{\sigma_y} \sin\alpha_n \tag{B.13}$$

Where $\sin\alpha_n = \frac{n\pi\sigma_0}{\sigma_y} \equiv s\sigma_0$

$$p = \sum_{\{n=1\}}^{\infty} \frac{2}{\sigma_y} \sin\alpha_n \exp\left[-\left(\frac{n\pi}{\sigma_y}\right)^2 \int_1^{\zeta} d\zeta' f(\zeta')\right] \sin\left(\frac{n\pi\sigma}{\sigma_y}\right)$$

$$\sum_{[n=1]}^{\infty} \rightarrow \int_0^{\infty} dn = \frac{\sigma_y}{\pi} \int_0^{\infty} ds$$

$$p = \frac{2}{\pi} \int_0^{\infty} ds\ \sin s\sigma_0 \exp\left[-s^2 \int_1^{\zeta} d\zeta' f(\zeta')\right] \sin(s\sigma) \tag{B.14}$$

Integrating the diffusion relation Eq. (B.5) with respect to $\boldsymbol{\sigma}$ gives,

$$\frac{\partial}{\partial\zeta} \int_0^{\infty} d\sigma p(\sigma,\zeta) = -f(\zeta) \frac{\partial p}{\partial\sigma}(0,\zeta)$$

Integrating the above equation by $\zeta$,

$$J' = 1 - \int_1^{\zeta} d\zeta' f(\zeta') \frac{\partial p}{\partial\sigma}(0,\zeta') \tag{B.15}$$

Substituting from equation (B.25),

$$J = \int_1^{\zeta} d\zeta' f(\zeta') \frac{\partial P}{\partial \sigma}(0, \zeta')$$

$$= \frac{2}{\pi} \int_0^{\infty} ds \ \sin s\sigma_0 \int_1^{\zeta} d\zeta' f(\zeta') \exp\left[-s^2 \int_1^{\zeta'} d\zeta'' f(\zeta'')\right] \sin(s\sigma)$$

$$J = 1 - \frac{2}{\pi} \int_0^{\infty} ds \frac{\sin s\sigma_0}{s} \exp\left[-s^2 \int_1^{\zeta} d\zeta' f(\zeta')\right] \quad \text{(B.16)}$$

Hence,

$$P(\zeta) = J' = 1 - J = \frac{2}{\pi} \int_0^{\infty} ds \frac{\sin s\sigma_0}{s} \exp\left[-s^2 \int_1^{\zeta} d\zeta' f(\zeta')\right]$$

Let $\boldsymbol{s\sigma_0 = x'}$. Then,

$$\boldsymbol{P(\zeta) = \frac{2}{\pi} \int_0^{\infty} dx' \frac{\sin x'}{x'} \exp\left[-x'^2 \int_1^{\zeta} d\zeta' g(\zeta')\right]; \quad g(\zeta) = \frac{f(\zeta)}{\sigma_0^2}} \quad \text{(B.17)}$$